An experimental study of trailing vortex dynamics on cruise and high-lift wing configurations

Rolando Cruz Marquez, Jean Claude Monnier, Geoffrey Tanguy, Patrick Dupont, Vincent Brion, Marie Couliou

An experimental study of trailing vortex dynamics on cruise and high-lift wing configurations

R. Cruz Marquez*, J. C. Monnier†, G. Tanguy‡, P. Dupont§
Univ. Lille, CNRS, ONERA, Arts et Metiers Institute of Technology, Centrale Lille, UMR 9014 - LMFL - Laboratoire de Mécanique des fluides de Lille - Kampé de Fériet, F-59000 Lille, France

V. Brion¶, M. Couliou‖
ONERA, University Paris Saclay, F-92190, France

Towing tank experiments are conducted to investigate the effect of the wing span-wise load profile on the structure and strength of trailing vortices. In the framework of the lifting line theory, the local circulation Γ_y (with y the span-wise coordinate) depends on the local chord, effective incidence and lift coefficient. For a commercial aircraft, the wing geometry varies depending on the phase of flight (eg. deployment of high-lift devices for take-off/landing) which modifies Γ_y. Theoretical models found in the literature allow to relate the configurations of trailing vortices about this span-load. However, few experimental validation exists for complex cases. The question of how a given span load influences the vortex wake structure and its dynamics is of high interest. Furthermore this question also relates to that of the wake control strategies. In this work, we investigate the wake dynamics resulting from two different span-loads to answer these questions. The baseline case is a NACA 4412 rectangular wing with no twist. A second model creates a load variation about this reference by twisting a specific inboard section. On top of the main external tip vortices, this introduces additional vortices downstream. SPIV measurements in sections of the wake generated by the towed wings are made to asses the vortex characteristics such as radius, circulation, swirl number and trajectory in each configuration. The development of the vortex wake is investigated from the roll-up stage up to 170 spans downstream at a chord based Reynolds number of $Re_c = 10^5$. In both wing configurations, the towing velocity U_0 and angle of attack α are modified to produce the same total lift as the baseline case and compare the distribution of downstream vorticity. In the case of the high-lift wing, the ratio of circulation between the flap and wingtip vortices is studied. Results show that at high α axial flow deficit grows. The swirl number decreases as a consequence but stagnates towards the value of 1.5 which is a threshold for instability onset. Under similar total loading conditions, vortices trailing behind the high-lift wing have a higher circulation, core size, and axial velocity than those of the untwisted wing.

Nomenclature

Ref	=	Untwisted wing (cruise configuration)
HL	=	Flaps-down wing (high-lift configuration)
α	=	wing geometric angle of attack [^{o}]
Θ	=	wing geometric twist [^{o}]
c_0	=	wing chord [m]
b_0	=	wing span [m]
b_f	=	wing span of a follower aircraft [m]
b	=	vortex separation [m]

*PhD candidate - rolando.cruz_marquez@onera.fr
†Research Engineer
‡Research Engineer
§Research Engineer
¶Research Engineer
‖Research Engineer

X, Y, Z	=	respectively stream-wise, span-wise and vertical directions [m]
U, V, W	=	respectively stream-wise, span-wise and vertical velocities [m/s]
x, r, θ	=	respectively axial, radial and angular directions [m]
N_r, N_θ	=	respectively radial and angular resolution of an interpolated grid
V_x, V_r, V_θ	=	respectively axial, radial and angular velocity [m/s]
W_d	=	Descent velocity of the vortex dipole [m/s]
θ^o	=	angle between a trajectory deformation and the traverse plane
ω_x	=	axial vorticity [s^{-1}]
$\overrightarrow{x}_{\overline{\omega}}$	=	location of the barycenter of vorticity in the measurement plane
$\overrightarrow{x}_{\Gamma 1}$	=	location of $\Gamma 1$ criterion in the measurement plane
δ	=	vortex position offset from an unperturbed trajectory [m]
$\overrightarrow{x}_{\max(U)}$	=	location of peak axial velocity in the measurement plane
ΔU	=	Axial velocity differential between the far-field ($r \to \infty$) and the vortex core ($r \to 0$) [m/s]
U_p	=	platform towing velocity [m/s]
U_0	=	constant velocity during towing [m/s]
dt	=	inter-frame separation time during SPIV measurement [s]
Δt	=	time separation between SPIV measurements [s]
t	=	elapsed time from the crossing of the SPIV plane by the wing [s]
T	=	non-dimensional time defined by the downstream station in the wake = $t * U_0/b_0$
T_c	=	non-dimensional time defined by the mutual induction of the vortices in the wake = $t\frac{\Gamma}{2\pi b^2}$
ℓ_y	=	local lift in a section of the wing [N/m]
F_z, F_x, F_y	=	respectively aerodynamic lift, drag and side forces [N]
L, M, N	=	respectively aerodynamic rolling, pitching and yawing moments[N.m]
C_z	=	lift coefficient = $\frac{F_z}{0.5\rho U_0^2 c_0 * b_0}$
C_x	=	drag coefficient = $\frac{F_x}{0.5\rho U_0^2 c_0 * b_0}$
C_R	=	rolling moment coefficient = $\frac{L}{0.5\rho U_0^2 b_0}$
ρ	=	density [kg/m^3]
ν	=	kinematic viscosity [m^2/s]
c_ω	=	vorticity criterion
R_ω	=	radius where axial vorticity is contained as $\overline{\omega}_x(r = R_\omega) = c_\omega * \max(\overline{\omega}_x(r))$ [m]
R_a	=	vortex core radius [m]
R_d	=	vortex dispersion radius [m]
Γ_y	=	local circulation on the wing [m^2/s]
$\Gamma(r)$	=	vortex circulation as a function of the radial distance [m^2/s]
Γ	=	vortex total circulation [m^2/s]
r_Γ	=	circulation ratio between main and secondary vorticity shed by a wing
q	=	Swirl number $q = \frac{\Gamma}{2\pi R_d \Delta U}$
Re_c	=	chord based Reynolds number : $\frac{U_0 * c}{\nu}$
Re_Γ	=	vortex Reynolds number : $\frac{\Gamma_0}{\nu}$
τ	=	length of the time window on a time average operation
$< X >_\tau$, $< X >_\theta$	=	respectively time and azimuthal average operator on the population X
$\overline{X}$	=	average operator between different realizations of an experiment for the population X
$std(X)$	=	standard deviation operator on the population X
$\Delta X/\Delta T$	=	linear rate of time-evolution for X
B	=	Acronym for the Batchelor vortex model

I. Introduction

Wake vortices trailing behind commercial airplanes pose a threat to air traffic. During a wake encounter, a rolling moment or a down-wash force can be induced upon the following aircraft. The degree of hazard is a function of the vortex strength and size, which are a bi-product of the lift generated by the leading aircraft [1][2]. One way to tackle this issue is to develop vortex alleviation techniques. The usual approach is to play on the intrinsic dynamics of systems

of multiple vortices to hasten their decay. Motivated by the above problem, groundwork on the stability of a vortex pair was early provided by Crow [3], as he carried out a stability analysis of a pair of vortex filaments and characterized the sinusoidal growing mode of perturbation that results from the interaction between the self-induced waves of a deformed vortex and the induced strain field caused by the opposite vortex, also known as the Crow instability. The wavelength is typically about eight times the spacing of the vortices. Later on Tsai & Widnall [4] investigated vortex pair instabilities with a wavelength comparable to the vortex core size. These result from the ellipticity of the vortex streamlines in the strain imposed by the other vortex, and also implies vortex modes interacting together with this strain. These instabilities are known as short-wave or elliptic instabilities. Among these two instabilities, the Crow instability is the one of most practical relevance, as it causes the largest deformations of the vortex core. On the far wake, these deformations lead to the linking of the vortices in the pair, with reorientation of the axial vorticity in perpendicular directions. Although linking does not constitute the final stage of the vortex dynamics, it is usually considered as a mark of the vortex lifespan in its original structure. Using a setting of flapping plates in a water tank Roy *et. al* [5] and then Leweke & Williamson [6] could characterize the growth rates and wavelengths of the long-wave and short-wave instabilities, in good agreement with theory. The same instabilities where characterized in co-rotating vortex systems by Meunier & Leweke [7]. Using a slotted wing apparatus Devenport *et. al* [8] and Brion & Jacquin [9] could clearly observe the Crow instability in wind tunnel experiments thereby replicating more closely an aircraft configuration.

Substantial efforts have turned towards the exploration of cooperative instabilities on systems of multiple vortex wakes. Towing tank experiments led by Ortega [10] proved the existence of unstable modes which, compared with the Crow mode, exhibited greater growth rates and smaller characteristic times in systems of 4 vortices. Similar analysis focused on the development of co-operative instabilities where performed by Crouch [11], Fabre & Jacquin [12] [13] and later Bristol *et al.* [14]. Essential parameters for the development of this phenomenon where found to be vortex spacing and the circulation ratio between vortex pairs. Durston *et. al* [15] explored multiple wing/tail vortices combinations on a similar experiment to determine promising configurations in terms of induced rolling-moment hazard reduction. Breitsamter *et. al* [16] performed wind tunnel experiments on a scaled 4-engine transport aircraft wing in high lift configuration to observe the interaction between the multiple vortices present in the wake. In this scenario flap and nacelle vortices quickly fuse forming a dominant vortex that eventually absorbs the wingtip vortex. It was shown that co-operative instabilities, namely the Crow and Crouch instabilities, are present in this remaining vortex system.

Another family of unstable modes stems from the presence of axial flow in the core of vortices. Trailing vortices with axial flow where described early-on by Batchelor [17] and Moore & Saffman [18]. Wake-type axial flow generates from the velocity deficit in the wing boundary layer and it is related to azimuthal velocity through the balance of pressure and centrifugal forces, making their study more representative of an aircraft wake. Pressure waves traveling in a columnar vortex have also been shown to cause the development of strong axial flow (Moet [19] and Meunier [20]). The dynamics of the Batchelor vortex are piloted mainly by the swirl number q, the ratio of azimuthal to axial velocities in the vortex. Furthermore the vortex becomes unstable at low values of swirl, as was first shown analytically by Lessen *et.al* [21] and Mayer & Powell [22]. The considered instability is called "helical" relating to the structure of the corresponding modes along the vortex axis (see [19] for a DNS visualization). Numerical studies like those of Delbende *et.al* [23] and Olendraru *et.al* [24] corroborated that the application of axial flow is an efficient means of promoting amplification of linearly unstable helical modes in wake type vortices. The development of the helical instability under these conditions was also observed through DNS and LES by Moet [19]. Beyond moderate swirl values ($q > 0.7$) Jacquin & Pantano observed the development of an annular *stable buffer layer* preventing the transport of perturbations in the vortex until ($q \approx 1.5$) where all helical modes fully dampen.

Various control techniques have been searched to hasten the decay of trailing vortices under constraints of applicability. The attempt to control them by actuation on the wing, passive or active, based on the known frequency of the wake instabilities has constituted one of the main focus. Indeed, the transport of perturbations from the wing surface to the vortex structure is evident in the framework of Prandtl's lifting line theory [25] where the span-wise distribution of lift is related to the shed vorticity profile in the wing near-wake. Rossow [26] generalized the Betz method [1] to get a simplified way of relating the span load data to the far wake vortex structure through the conservation of invariant quantities in the flow but neglecting essential phenomena as the fusion and roll-up processes, viscous decay, atmospheric turbulence and eventual instabilities.

An overview of experimental studies focusing on the reduction of trailing vortices lifespan is provided by Spalart [27], Gerz [28] and Savas *et.al* [29]. Defining the best location or control shape to actuate requires the use of models, theories and simulation capable of describing the dynamics of small perturbations imposed to the main flow. The outcome is potentially a much better efficiency of the control, yet with difficulties when transposing theoretical results to experimental practice. Along this line Brion *et al.* [30] focused on characterizing the zone of sensibility for the

excitation of the Crow instability on a vortex dipole. Based on recent work on linear stability analysis (Edstrand *et.al* [31]) and transient growth (Navrose *et.al* [32]), Cruz Marquez *et. al* [33]modified the trailing edge of a NACA 0012 rectangular wing into a sinusoidal shape to perform an experimental study of the theoretical excitation. A diffusive effect on the vortex core was obtained 60 wingspans downstream on the wake, but the vortex total circulation was unaffected. A more diffused vortex core was also obtained in experiments by Dghim *et.al* [34] and by Guha & Kumar [35] through active flow control. In refs. [34] and [35], it is shown that the perturbations introduced over the wing surface also travel considerable downstream distances. The wake hazard is alleviated, but the control strategy (passive or active) does not bring a significant change in the wake dynamics which are necessary to bring about the excitation of flow instabilities and accelerated vortex decay.

In the present work experiments with wing models of various span-wise lift distributions are conducted at ONERA towing tank to address some of the unresolved issues on the impact of the load profile on the dynamics of the vortex wake. Experiments focus on two wings where the span-wise evolution of geometrical twist is modified to compare the dynamics of wake vortices in configurations representative of cruise flight and landing/take-off. The studied wakes will be characterized in terms of magnitude and time-evolution of the vortex strength, size and swirl. The impact of the flight configuration on the rolling moment induced on a follower aircraft will thus be defined. These results will also provide experimental data for the validation of analytical models.

II. Experimental setup

A water towing tank experiment equipped with stereo-particle image velocimetry (SPIV) measurement is used to study the development of the vortex wake of a rectangular wing up to 170 spans downstream (Fig.2). A detailed description of this experimental installation can be found in Cruz Marquez *et. al* [33]. The reference frame is as follows: The wing is towed in the longitudinal direction X. We denote as left side and right side the negative and positive $Y-$coordinates, respectively. This will be used to designate the two vortices composing the wake. The vertical direction Z is positive upwards.

A. Wing model

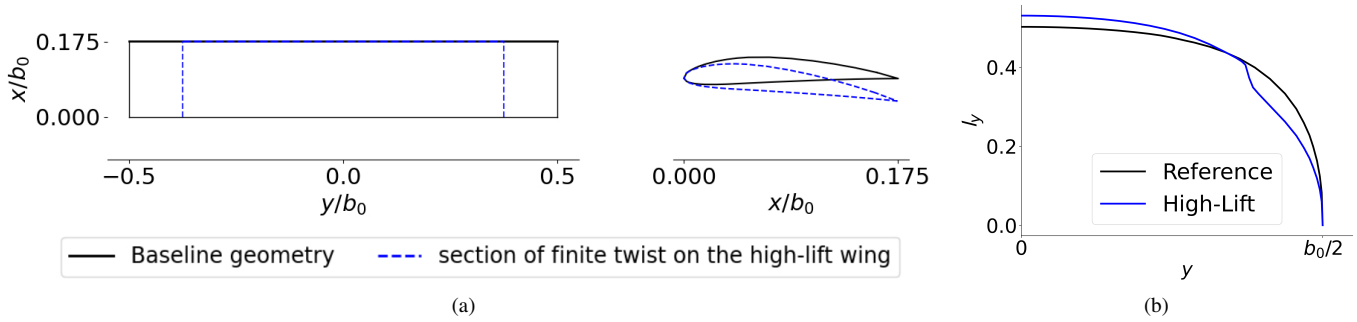

(a) (b)

Fig. 1 (a) Top and side schematics of the geometry and (b) wing load panel method results on ℓ_y as a function of span-wise station at iso-aerodynamic loading for the reference ($U_0 = 5m/s$, $\alpha = 2.125^o$) and high-lift ($U_0 = 3.75m/s$, $\alpha = 1.75^o$) wing models.

The baseline wing geometry is rectangular with a NACA 4412 profile. The chord and span are $c_0 = 0.07\ m$ and $b_0 = 0.4\ m$, respectively, which results in an aspect ratio of 5.7. Experiments are carried out on a range of wing geometric angle of attack $\alpha \in [1^o : 5.7^o]$ and towing velocity magnitude $U_0 \in [1\ m/s : 5\ m/s]$. The wing is held at mid-span by a strut of chord c_0 and NACA 0015 profile. The alignment of the wing and strut with the towing direction was controlled using the SPIV data to obtain the best symmetry of the wake flow.

The span-wise loading profile on the wing serves as a design guideline since it can be related to the structure of the trailing vortices in the far-wake [26]. Let y be the span-wise station along the lifting surface and $\Gamma_y(y)$ the local circulation at that same cross section determined by wing geometry and effective angle of incidence. The loading profile $\ell_y(y)$ is the span-wise evolution of the local lift $\ell_y = \rho U_0 \Gamma_y$. For most applications, lifting line theory is sufficient to accurately determine ℓ_y. For the purposes of this work, two wing models were designed. Top and side views of the

wing geometry is schematized in Fig. 1a. The load profile corresponding to each wing model is provided on Fig. 1b.

On the first model, the span-wise distribution of geometrical twist angle Θ is kept to zero. This untwisted rectangular planform generates a loading profile close to the elliptic law (see Fig. 1b). This wing model is more representative of cruise flight, since during this phase an aircraft wings are plain. In this work, this geometry provides a reference case and is referred to by the subscript *Ref*.

The second model has a constant twist value $\Theta = 6^o$ from the mid-plane to $y = 0.375b_0$. For the outboard section, from $y = 0.375b_0$ to $y = 0.5b_0$ (the wing-tip), the twist angle is $\Theta = 0^o$. Similar to the aircraft *high-lift* wing configuration where the inboard wing flaps are deployed at ground proximity to generate additional lift, on this wing model the twisted section covers 75% of the total wing-span. On the ℓ_y curve, this translates to higher loading values on the inboard section of the wing (see Fig. 1b). Past the $y = \pm 0.15$ position, the loading curve follows the reference elliptical profile. The evolution of Θ from the outboard to the inboard region is discontinuous due to construction constraints. This wing model is designed to be representative of the flaps down wing configuration of a commercial airplane during landing phase and it is therefore referred to by the subscript *HL*.

The towing velocity U_0 is used as velocity scale to characterize the evolution of the wake. The wing-chord c_0 and wingspan b_0 are used as reference lengths to characterize, respectively, the flow past the wing and the wake. The transition from one normalization system to the other is made through the wing aspect ratio. The flow past the wing is characterized by the chord based Reynolds number of $Re_c = U_0 c_0/\nu$ with ν the kinematic viscosity of the water. In the range of towing velocities of this work, the chord based Reynolds number ranges from $Re_c = 8.8 \times 10^4$ to $Re_c = 4.4 \times 10^5$. We further introduce the vortex Reynolds number Re_Γ based on the circulation Γ of the vortices of the wake. The calculation of Γ is detailed in III.A.5 for which Re_Γ is about 8×10^4.

B. Towing tank facility

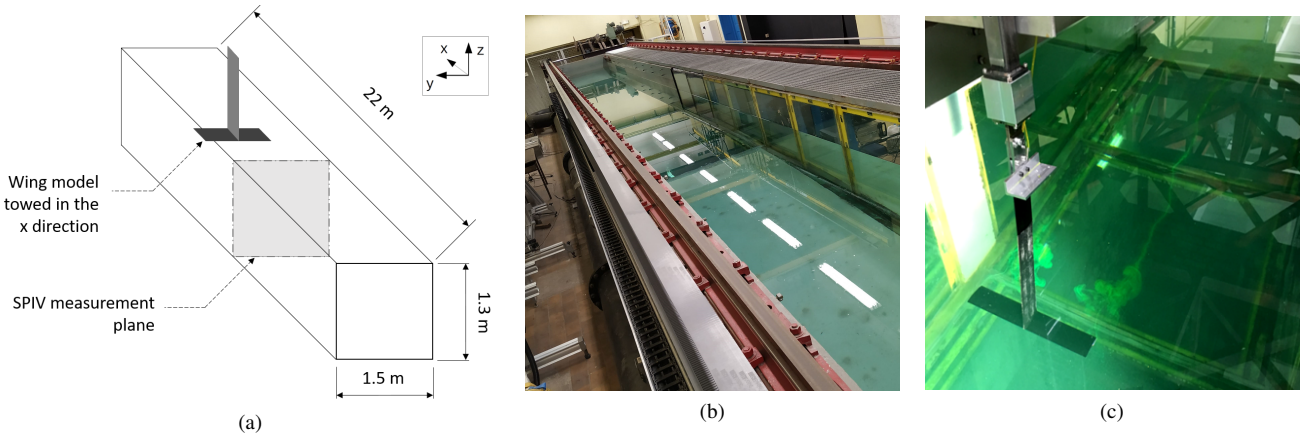

(a) (b) (c)

Fig. 2 Towing tank installation equipped with SPIV measurements : a) Installation overview b) Towing tank and c) Wing model during towing.

The towing tank facility is installed in the ONERA Lille research center in northern France. The tank features a full length of 22 m, a width of 1.5 m and a depth of 1.3 m, yielding normalized values of 55, 3.75 and 3.25 in b_0 units respectively. The tank is filled with water and the height of water is maintained constant throughout the test campaign. The water is also filtered to remove unwanted particles. The experimental facility is schematized in Fig.2a. Photographs of the tank and wing model in it are shown in Fig.2b and 2c.

The wing is immersed at a depth of 0.5 $m = 1.25b_0$ below the surface of the water, that represents an altitude of $2.16b_0$ above the tank bottom surface. The distance between the model and the tank lateral and bottom boundaries is $1.28b_0$ and is sufficient to avoid any significant wall-induced effects [16]. The vertical strut holding the wing is connected to a *AMTI MC3A* 6-components force balance and the balance is attached to the towed platform (Fig.2c). The force sensor is described further down. The platform translates on rails over a towing distance of 18 m. We stress that the towing motion does not generate vibrations neither to the model nor to the flow. For an experiment where the target towing velocity is $U_0 = 2\ m/s$, the evolution of platform speed U_p as a function of the axial coordinate X, is shown in Fig.3a. The duration of the initial and final phases (acceleration and deceleration) are chosen so as to maximize the

intermediate phase of constant speed of magnitude U_0. The resulting temporal evolution of the longitudinal position $X(t)$ of the wing during an experiment is shown in Fig.3b with the lower and upper axis respectively indicating time t in seconds and in non-dimensional time T normalized by the b_0 and U_0 based convection time and given by

$$T(t) = t\frac{U_0}{b_0} \tag{1}$$

T is useful when analyzing the characteristics of the vortex from the near field to the far field defined by the limits of the towing tank experiment. Note that this time scale is analog to the downstream station in the wake, counted in wingspans b_0. The towing length and acceleration phases dictate the temporal duration of the vortex wake experiment in the measurement plane located at approximately the mid-length of the tank. Specifically the abrupt start and stop of the wing generates vortex waves in the trailing vortices that disturb the experiment when these waves reach the measurement plane. These waves are known to travel at approximately the maximum azimuthal velocity in the vortices, an estimation of which yields $U_\theta/U_0 \simeq 0.175$ for a towing motion at $\alpha = 5^o$ and the velocity conditions represented in Fig.3. With the half length of the tank being about $25b_0$, the duration of the measurement is estimated to be about 140 normalized units.

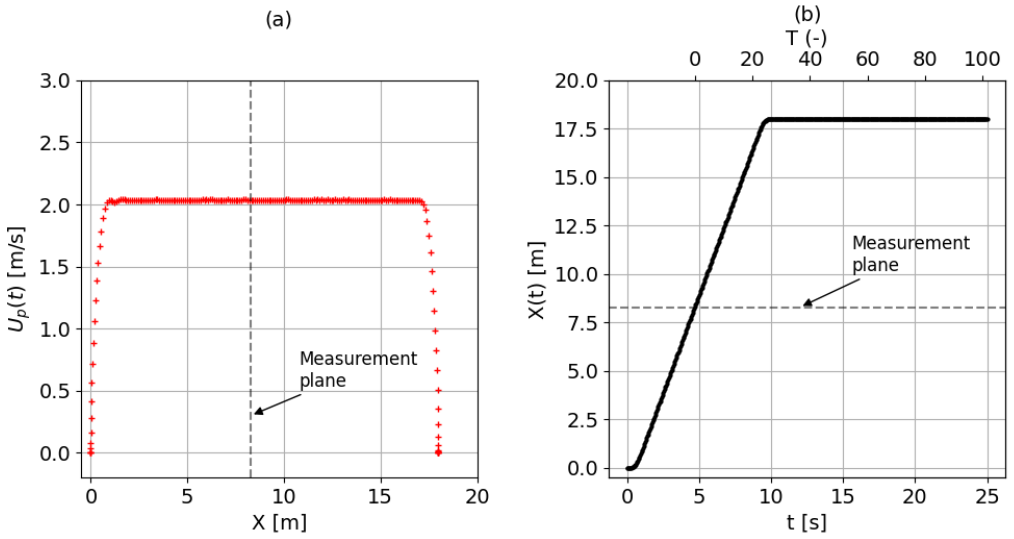

Fig. 3 Characteristics of the towing motion on an experiment of target velocity $U_0 = 2m/s$: a) towing velocity U_0 as a function of the longitudinal position X in the canal and b) longitudinal position X as a function of time t and non-dimensional time T.

C. Aerodynamic force measurements

Aerodynamic forces (F_z, F_x, F_y) and moments (L, M, N) generated by the wing are measured using a 6-component force sensor mounted as detailed previously. The vertical and horizontal components on the force sensor have a saturation threshold of 1100 N and 550 N respectively. During the experimental campaign, the towing configuration (U_0 and α) is chosen so as to generate aerodynamic forces under this threshold value. The force signals are sampled at a rate of 5000 Hz. The recording is started after the towing acceleration phase and stopped at the end of the course (see Fig.3). The moving average of the forces and moments generated by the wing are found to be constant during the constant velocity phase, indicating satisfactory stationary conditions in this phase. The standard deviation of the force measurements is on an order $< 1\%$ of the averaged value. Random drift of the force sensor is corrected using data recorded before the beginning of the platform movement. The drag of the wing is obtained after having subtracted the drag due to the strut, which was measured in a preliminary step, when no wing is attached (the interference effect between the strut and the wing is neglected). Lift and drag measurements obtained by this method are provided further down in Fig.15. Aerodynamic lift and drag coefficients are then computed as

$$C_{Z,X} = \frac{F_{Z,X}}{0.5\rho U_0^2 b_0 c_0}$$

D. SPIV measurements

1. Data acquisition

Stereo PIV measurements of the flow are realized in the measurement plane. A front view of the installation is given in Fig.4a. The SPIV setting operates at a frequency of $f = 5$ Hz. In the chosen towing velocity range $U_0 \in [1\ m/s : 5\ m/s]$, the snapshot recording frequency corresponds to a normalized value of $fb_0/U_0 = 2$ and 0.4 respectively for the for the lowest and highest velocities. The sensor size of the cameras and field of view generates a field with a spatial resolution of 0.0013 m corresponding to $0.00325b_0$.

The vortex wake descends upon mutual induction at a velocity W_d. The configurations that lead to the lowest and highest vortex velocities are respectively ($U_0 = 1\ m/s, \alpha = 0^o$) and ($U_0 = 5\ m/s, \alpha = 5^o$). The combination of SPIV sampling rate and spatial resolution leads to a wake descent that is, respectively for the lowest and highest velocities, 0.6 and 6.0 grid points per measurement. Non-dimensional time normalized by the time scale of the vortices mutual induction [3] is defined as

$$T_c(t) = t\frac{\Gamma}{2\pi b^2} = t\frac{W_d}{b} \tag{2}$$

where b is the separation of the vortices in the wake. The SPIV sampling rate leads to, respectively for the slowest and highest velocities, $\Delta T_c(0.2) \approx 0.002$ and $\Delta T_c(0.2) \approx 0.021$. Hence this downward motion is well captured.

The computation of W_d and b are detailed in section III.A.2. Additional information on the spatial and temporal resolution relative to the wake descent is provided in table 1.

The water tank is seeded with polyamid seeding particles of diameter 20 μm and density $\rho_p = 1.03\ g/cm^3$ which have shown to provide good measurement results in similar water tank experiments [36]. A top view of the measurement setup is provided in Fig.4b. With one camera at each side of the plane, two consecutive images are acquired by both cameras in the SPIV plane. A specific inter-frame separation time dt is chosen as a function of U_0. dt values are presented on table 1.

U_0 **(m/s)**	1.0	2.0	3.0	4.0	5.0
Re_c	8.8×10^4	1.8×10^5	2.6×10^5	3.5×10^5	4.4×10^5
dt (ms)	7.5	3.8	2.5	1.8	1.5
Δt (s)	0.2	0.2	0.2	0.2	0.2
$T_c(\Delta t)$	0.002	0.004	0.006	0.008	0.011
$T(\Delta t)$	0.5	1.0	1.5	2.0	2.5

Table 1 Chord-based Reynolds number and time scales for experiments at an angle of attack $\alpha = 0^o$ as a function of towing velocity U_0

The images are captured by two LaVision sCMOS cameras equipped with $f = 35$ mm lenses and the laser sheet is generated by a 380 mJ Nd:YAG laser system. The ONERA FOLKI [37] software is used to reconstruct the velocity fields $\vec{V} = (U, V, W)$, which uses a modified iterative wrapping scheme analog to the dense Lucas-Kanade algorithm [38].

The SPIV acquisition is automatically triggered when the wing passes a gate located upstream of the measurement plane. Note that the activation time trigger erroneously differs between runs, which leads to a time separation of $|\Delta T| < 0.5$ between experiments. However, due to the small value, we consider that it has a negligible effect on the data and analysis results.

E. Bounds of the SPIV window

The size and location of the SPIV measurement window are shown in Fig.4a. The width of the SPIV window is $1.45b_0$. It is related to the camera viewing angle, which is 37^o. A top view of the measurement installation is given in Fig.4b. The viewing angle is set by the incident angle of prisms installed between the cameras and the PMMA window. These water-filled prisms compensate for refraction angles on the optic path between the immersed particles and the cameras.

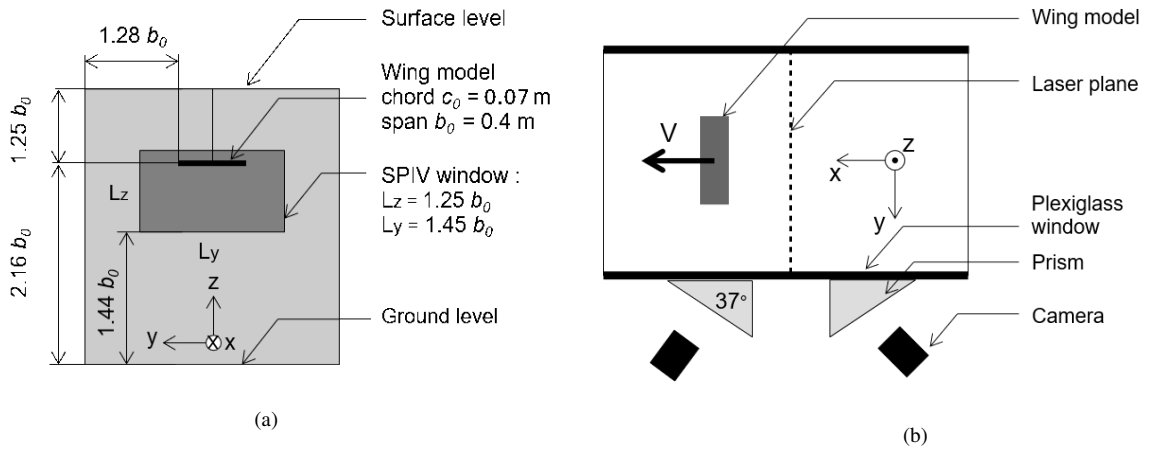

Fig. 4 SPIV measurement installation : a) Tow tank cross-section at the location of the SPIV plane b) SPIV installation top-view.

The window contains the entire wing wake and allows for the capture of its descent down to a height equal to $1.44b_0$ above the tank bottom surface. As the vortices reach this boundary, part of their velocity and vorticity fields exit the SPIV domain and put a halt to the analysis of the flow.

An illustration of the flow dynamics observed in the SPIV window for the baseline case at $\alpha = 3^o$ and $U_0 = 5\ m/s$ is shown in Fig.5 using fields of the velocity magnitude V_M defined as

$$V_M = \sqrt{U^2 + V^2 + W^2} \tag{3}$$

We use a specific coordinate system centered about the wing Y-plane of symmetry. Fig.5 shows the flow field at 4 successive time instants and indicates the typical velocity magnitude V_M in the vortices, which is approximately 20% of the towing velocity. The descent of the wake is clearly visualized, with little variation of the vortices magnitude during the chosen duration.

For all experiments realized in this work, two fairly defined vortical structures are observed from the first measurements taken after the passage of the wing through the SPIV plane. This is in agreement with theoretical [39] and experimental [16] studies for which the vorticity sheet shed by the trailing edge is expected to concentrate into defined structures before $T = 0.5$. Defined vortical structures are observed through the rest of the measurements until the moment they exit the SPIV window through their vertical descent. Therefore, no bursting nor any other loss of structure of the vortices is observed before they exit the measurement window. The maximum vortex ages measured in our experiments are summarized in table 2. For most configurations, the maximum age is under the threshold for which any significative development of cooperative instabilities is expected to emerge between the vortices and cause their dispersion [3] [16].

$U_0\ m/s$	1.0	5.0
$\alpha = 0^o$	134 (**0.59**)	170 (**0.74**)
$\alpha = 5^o$	79 (**0.63**)	75 (**0.64**)

Table 2 Maximum vortex age measured before the exit of the vortex of the SPIV window in terms of T and in terms of T_c (inside parenthesis) as a function of angle of attack α and towing velocity U_0

It must be noted that the optical arrangement of the SPIV measurements has resulted in a degradation of the velocity field data retrieved by the SPIV between the right and left sides of the flow. We make the conservative choice of focusing our analysis on the right side vortex, which is less affected by this degradation. The symmetry of properties in the vortex is assumed by considering the symmetry of both vortices trajectories (see sec. III.A.2). Further details on this procedure are provided in Cruz Marquez *et. al* [33].

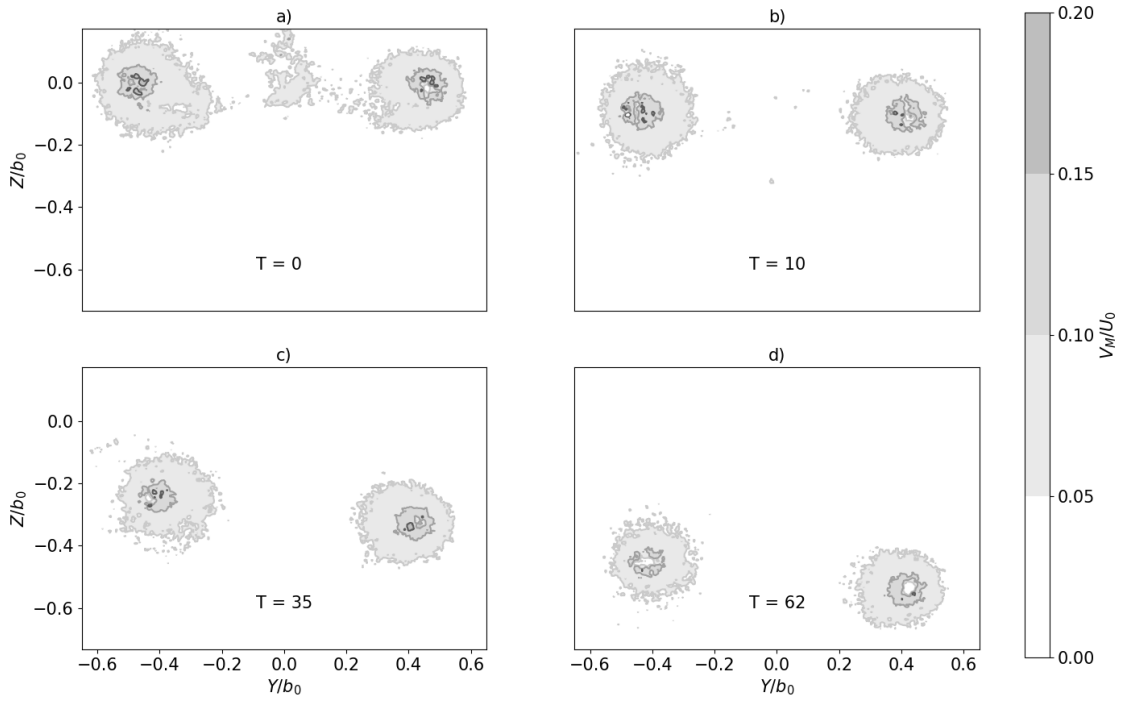

Fig. 5 Non-dimensional velocity magnitude V_M/U_0 on the wake of the baseline wing configuration. Elapsed non-dimensional time T, corresponding to different downstream locations are represented.

III. Results

A. Baseline wing configuration

This section describes the results obtained for the baseline configuration. The main characteristics of the vortex system are computed and analysed.

1. Velocity field induced by the wake

The velocity field that the trailing vortices of a leader aircraft induces on a following aircraft is composed of an induced rolling moment and induced lateral, up and down-wash forces. It is of interest to evaluate the relationship between vortex characteristics (namely core size R_a and circulation Γ) and the induced velocity field. Thereafter, the subscript f refers to the following aircraft. For practical considerations, let $b_f = b_0/2$ and $U_f = U_0$.
A field of rolling moment coefficient and down-wash force induced by a wake of two counter-rotating vortices is shown in Fig. 6. The wake is symmetric with respect to the mid-plane ($Y = 0$). Vortices are located in $y_{c,1} = +b_0/2$ and $y_{c,2} = -b_0/2$. The vortices have a Lamb-Oseen profile with input non-dimensional circulation and core values similar to that of cruise flight. In the framework of thin airfoil theory, the resulting C_R is a function of the section lift l induced at every span-wise station of the wing, expressed in terms of induced vertical velocity V_z [2], yielding :

$$C_R = \frac{2\pi}{U_0 b_f^2} \int_{y_f - \frac{b_f}{2}}^{y_f + \frac{b_f}{2}} (y - y_f) \left(V_{z,1}(y, z_f) + V_{z,2}(y, z_f) \right) dy \tag{4}$$

As expected, C_R is maximum when the aircraft is aligned with the vortex axis. The expression of C_R in this location, first derived by Condit & Tracy [2], can be developed for vortices of arbitrary structure [40]. This yields for the Lamb-Oseen vortices in Fig. 6 :

$$C_R = \frac{\Gamma}{b_f U_0} \left(1 - \frac{\sqrt{2\pi}}{2.24} \frac{R_a}{b_f} \right) \tag{5}$$

Relation 5 shows that for a follower aircraft of fixed span, the induced rolling moment can be reduced either by

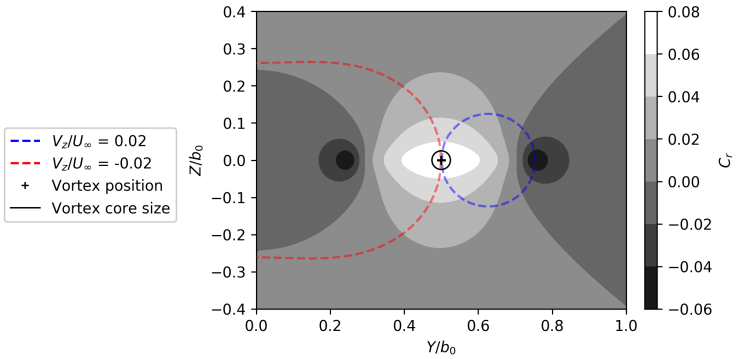

Fig. 6 Field of rolling moment coefficient C_R and up/down-wash forces induced by a wake on a following aircraft of span $b_0/2$. The wake is symmetric about $Y = 0$ and is composed of two Lamb-Oseen vortices positioned at $(\pm 0.5 b_0, 0)$. Up-wash and down-wash iso-contours are indicated, respectively, by blue and red dashed lines.

lower vortex circulation or by enlarging the upstream vortex core. Furthermore, it can be shown that the sensitivity of the induced rolling moment to the core size is a function of the ratio $\frac{R_r}{b_f}$. For a classical flight configuration where $R_r = 0.03 b_0$ and $b_f = \frac{1}{2} b_0$, doubling the vortex core size brings about a reduction of 5% in C_R. Besides the maximum C_R zone in the vortex core, a significant rolling moment and down-wash are induced at a half span distance from the core size, $|R_a + b_f/2|$ (see Fig. 6).

As seen in Fig. 6, a follower aircraft situated in the region between both vortices is affected by significant down-wash on top of the induced rolling moment. The value of the induced down-wash is inferred directly from $V_{z,1} + V_{z,2}$. For aircraft wake configurations, this value is maximum at the vortex core distance and yields $V_z(0,0) = \frac{\Gamma}{2\pi b}$ at the mid-plane of the wake.

2. Identification of the vortex center

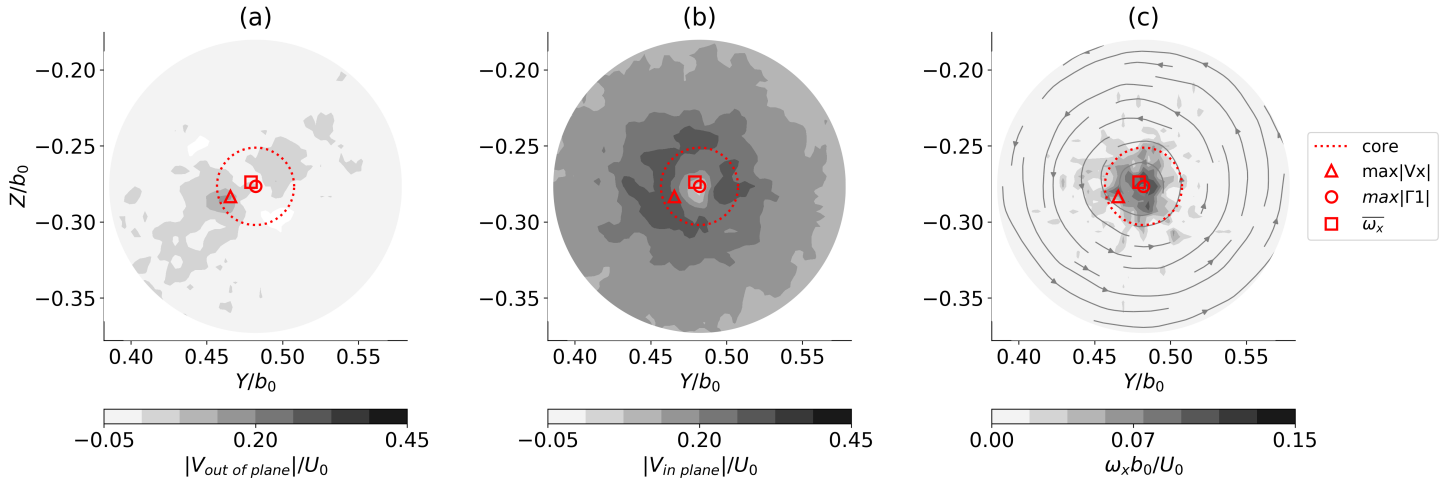

Fig. 7 Location of the vortex center defined by different criteria for the right side vortex trailing 33 wingspans downstream of the reference wing towed at $U_0 = 2\ m/s$ and $\alpha = 3^o$

The vortex center is identified using the SPIV data through two different approaches. On one hand we consider the barycenter $\overrightarrow{x}_{\overline{\omega}}$ of the axial vorticity field $\omega_x(y,z)$. The integration for the barycenter is computed over a reduced region centered about the maximum of axial vorticity $\max(|\omega_x(\overrightarrow{x})|)$ which is taken at the vertices of the SPIV mesh. From the trajectory of $\overrightarrow{x}_{\overline{\omega}}$ (further described below) the descent velocity W_d is obtained. On the other hand we consider $\overrightarrow{x}_{\Gamma 1}$ the vortex center defined by the $\Gamma 1$ criterion [41]. This criterion relies on the rotation rate of the in-plane velocity field

$\vec{V}(y,z) = (0, V, W)$ around a given vertex of the SPIV mesh. Since this criterion is not Galilean invariant, the descent velocity W_d of the vortex pair is subtracted before evaluating $\Gamma 1$ in the velocity field. Further details on this method can be found in Graftieaux *et. al* [41]. The implementation of this method into our towing tank experiments is further described in Cruz Marquez *et. al* [33].

The location of $\overrightarrow{x}_{\omega}$ and $\overrightarrow{x}_{\Gamma 1}$ on a SPIV vortex field is shown in Fig. 7. The measured fields of instantaneous out-of-plane velocity, in-plane velocity and axial vorticity are respectively represented in Fig 7a, b and c for the same value of T. The streamlines of in-plane velocity are represented in Fig. 7c. For clarity, all fields have been zoomed-in to $Y, Z \in [\overrightarrow{x}_{\Gamma 1} - 0.2b_0, \overrightarrow{x}_{\Gamma 1} + 0.2b_0]$. $\overrightarrow{x}_{\omega}$ and $\overrightarrow{x}_{\Gamma 1}$ give comparable results as they are both based in the in-plane velocity data. For all experiments, it was observed that $\overrightarrow{x}_{\Gamma 1}$ is, however, more subjected to clustering on the measurement grid points. The location of the peak of axial velocity $\overrightarrow{x}_{\max(U)}$ is also represented in Fig. 7. Contrary from what is expect by theoretical vortex models, we note that there is a mismatch between the vortex centroid $\overrightarrow{x}_{\Gamma 1}$ and $\overrightarrow{x}_{\max(U)}$. For the field shown in Fig. 7, the total shift observed is $0.018b_0$ m and is in the same order of magnitude as the vortex core size R_a (the computation of which is detailed in section III.A.5).

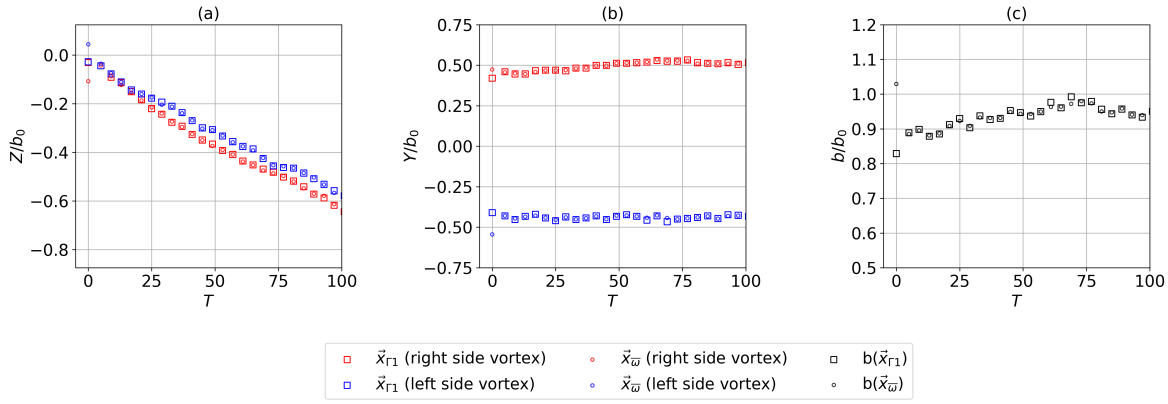

Fig. 8 Centroid trajectories $\overrightarrow{x}_{\Gamma 1}$ and $\overrightarrow{x}_{\omega}$ for the vortices generated by the reference wing towed at $U_0 = 2$ m/s and $\alpha = 3^o$

The trajectories of the two wake vortices are shown for the Z component in Fig.8.a and for the Y component in Fig.8.b. The vortex separation distance b is also shown (Fig.8.c). For clarity, data points on the figure have been decimated by 4 compared to the available data. Both centroid criteria give comparable results for the vortex trajectory except during the first stage of formation of the wake ($T \approx 0$) where vorticity can be broadly distributed. Furthermore, for both criteria, the observed rate of descent of the vortex dipole is identical. There is, however, a slight asymmetry between the left and right side trajectories, with the right side vortex descending at a faster rate. The vortices show a rectilinear descent along Z at a constant speed after a very short transient phase at initial time. For most experiments, during the initial transient phase vortices quickly translate from the wingtip span-wise station to an inboard zone defined by b/b_0.

For all tested configurations of U_0 and α, the measured ratio b/b_0 is superior to $\pi/4$, which is the theoretical value for an elliptic loading profile [42]. For all experiments, the trajectory of the dipole remains vertical even at the bottom of the SPIV domain. This indicates that the effect of the image vortices about the ground is negligible. In the case of a significant interaction with the ground, one could expect vortices outward motion [43].

The subsequent positions $\overrightarrow{x}_{\omega}(t)$ of the right side vortex trailing behind the reference wing at $U_0 = 2$ m/s and $\alpha = 3^o$ are shown in Fig. 9a. The time step between a position and the next is $\Delta t = 0.2s$ and $\Delta T = 1.0$. The position data is broken down in horizontal and vertical trajectories (see Fig. 9b) revealing a low frequency oscillation about the straight trajectory that the vortex would follow in an unperturbed case. A linear regression is used to estimate this ideal trajectory. Offset δ about the ideal trajectory is in the order of magnitude of the core size R_a. An FFT algorithm is then used to calculate the wavelength of the vortex motion. For the case shown in Fig. 9, the FFT yields $\lambda_x = 100b_0$. A dominant long wavelength λ_x was obtained in most experiments ranging in $\lambda_x/b_0 \in [39, 170]$. In some experiments, the large value of λ_x prevents the completion of a full oscillation period before the vortex exits the SPIV window. This deformation entails a rotation of the vortices around their axis, as shown by the time evolution of the angle $\theta^o = tan^{-1}(\frac{\delta_z}{\delta_y})$ between the horizontal plane and the deformation (see Fig. 9c). Therefore the deformation is related

to the induced and self-induced rotation rates of each vortex tube in the pair. The presence of self-induced rotation also shows that the Crow instability, if present, is in an early stage of development, as the fully fledged phenomenon is characterized by the "fixation" of the vortex deformation at an angle of $\theta^o \approx 47^o$. The nominal wavelength for the Crow instability (for elliptical loading) is $\lambda_{Crow} = 6.8b_0$ [3] which is an order of magnitude lower than that detected in the experiment. However, as shown in table 2 experiments with a larger time horizon should be performed to observe a significant development of Crow instability. In the time range of our experiments, if cooperative instabilities are present, they might have an amplitude too low to be detectable with the available frequential and spatial resolution.

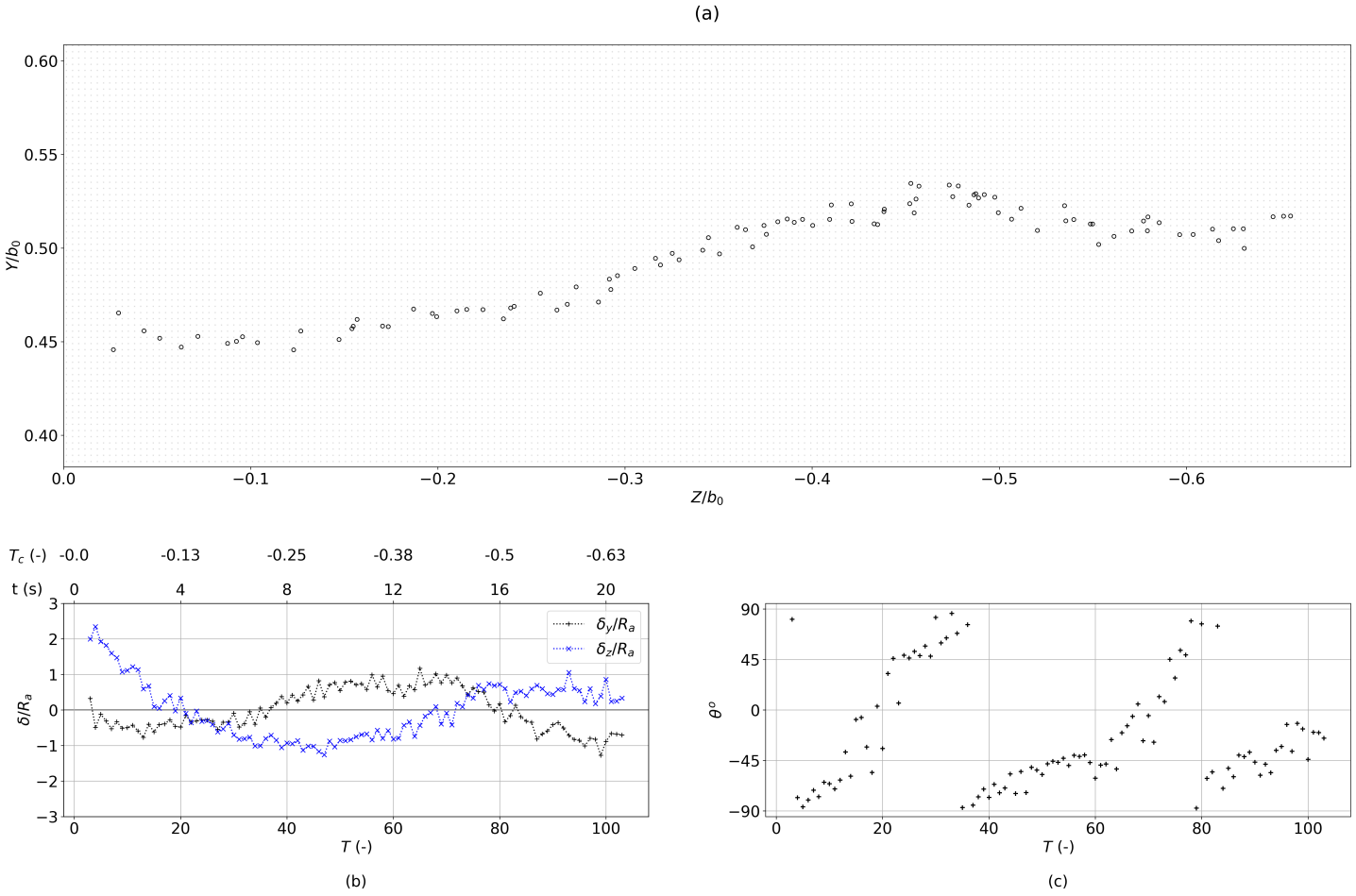

Fig. 9 Centroid trajectory $\vec{x}_{\overline{\omega}}$ for the vortices generated by the reference wing towed at $U_0 = 2$ m/s and $\alpha = 3^o$ a) trajectory in the (y, z)-plane b) offset of $\vec{x}_{\overline{\omega}}$ with respect to the unperturbed trajectory as a function of time t, non-dimensional time T, and Crow time T_c. c) time evolution of the angle between the deformation and the horizontal plane.

3. Vortex velocity field

The SPIV measurements of the stream-wise, span-wise and vertical velocities, U, V, W are provided in Fig.10a, Fig.10b and Fig.10c, respectively. The fields are zoomed-in to $Y, Z \in [-0.2b_0, 0.2b_0]$ and centered about the vortex center for clarity. A significant wake-type stream-wise velocity U, of peak value approximately $0.05U_0$ is observed in the core of the vortices, as shown in Fig.10a. Over time, the peak value of axial velocity for the reference wing ranges in $[0.05, 0.15]U_0$ as it will be shown further down. Similar values of wake-type axial flow have been reported in other experimental [16] and analytical works [17] and are related to the velocity deficit originated in the wing boundary layers. The vertical velocity W plotted in Fig.10c is corrected of the uniform vertical velocity field W_d that corresponds to the wake descent. The latter is calculated from the centroid displacement data shown in Fig. 13a.

In the following the velocity field of the vortex is more closely investigated and recast into a cylindrical coordinate system about the vortex center obtained by the Γ_1 criterion. The main aspects of this procedure are summarized on the following given that a more detailed description is provided in Cruz Marquez *et. al* [33]. The azimuthal and radial velocities, V_θ and V_r are shown in Fig.10d and in Fig.10e, respectively. The data on the polar grid is interpolated from that on the original cartesian grid (given by the SPIV) using the $\Gamma 1$ criterion for the instantaneous center as it was observed that this criterion maximises the symmetry of the resulting vortex flow [33]. The domain is limited to the radial distance $r_{max} = 0.4b_0$ which is a conservative value shorter than the midplane. The polar and azimuthal grid resolutions, respectively N_r and N_θ, are chosen so as to maintain approximately the same number of grid points in the core as the original SPIV grid, that is around 10 for the flow parameters represented in Fig. 10 [44],[45]. The azimuthal velocity field V_θ, shown in Fig.10d, is mostly axisymmetric about the vortex center. The maximum azimuthal velocities are a function of the angle of attack (see section III.B) and range from $0.075U_0$ to $0.175U_0$ for the experiments with the reference wing. In Fig.10e, the radial velocity field V_r remains at negligible values in most of the vortex domain, as would be expected. A residual radial velocity field is thought to result from the unavoidable slight error made in detecting the vortex core.

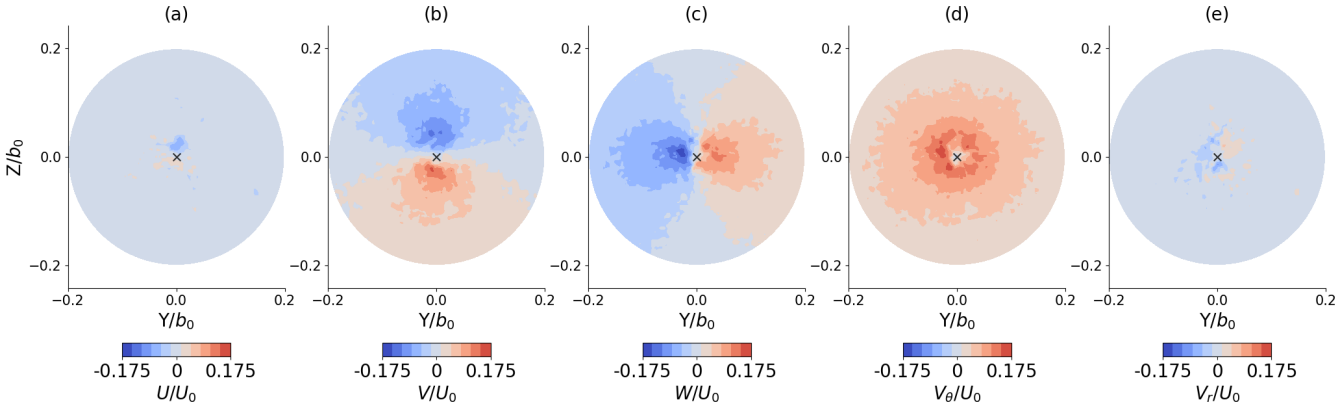

Fig. 10 a) U/U_0 **field b)** V/U_0 **field c)** W/U_0 **field d)** V_θ/U_0 **field e)** V_r/U_0 **field for the reference wing (**$U_0 = 5\ m/s$ **;** $\alpha = 3^o$**), 22 wingspans downstream in the wake. The reference frame is centered on the** $\vec{x_{\Gamma 1}}$ **criterion (black cross).**

4. Averaged velocity profile

An overall procedure of velocity averaging is performed to allow a fine characterization of the vortex parameters like radius and circulation. With the velocities being now expressed in the polar coordinates, azimuthal averaging can be carried out. This is indeed useful to qualify the vortex profile as a function of the radial distance. Several other averaging are done and detailed in this section using the example of the component V_θ. The same procedure is realized for the 3 velocity components, V_x, V_θ and V_r.

A snapshot of the velocity field $V_\theta(r, \theta, T)$ is represented in Fig. 11a. The first step of the procedure is to calculate $< V_\theta >_\tau$, a sliding time average velocity field using finite time windows $T_\tau = [T - \frac{\tau}{2} : T + \frac{\tau}{2}]$, following

$$< V_\theta(r, \theta, T) >_\tau = \frac{1}{\tau} \sum_{T_i = T - \frac{\tau}{2}}^{T + \frac{\tau}{2}} V_\theta(r, \theta, T_i) \tag{6}$$

This operation is performed to filter the unsteadiness between successive instantaneous flow fields. The value of τ is expressed in non-dimensional time units and is defined with respect to the diffusion time scale of the vortex. In this work, the value of $\tau = 5$ is considered sufficient for the viscous diffusion of the vortex to be negligible compared to the duration of the time window used in equation 6 [33]. In what follows, we use the notation $< X >_\tau$ to refer to the sliding time average operation with $\tau = 5$. $< V_\theta >_\tau$ is visible in Fig.11b and the standard deviation resulting from this mean is visible in Fig.11c.

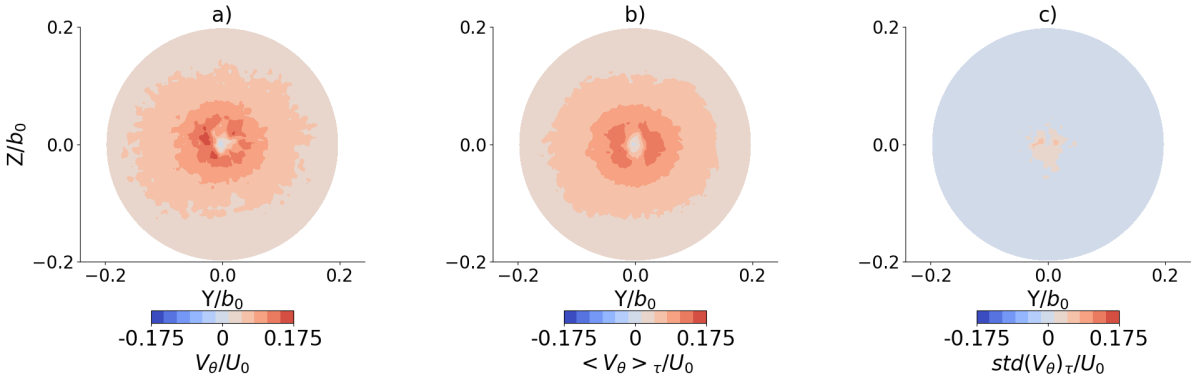

Fig. 11 a) Instantaneous velocity field $V_\theta(r,\theta,T)/U_0$, b) time-averaged ($\tau = 5$) velocity field $< V_\theta(r,\theta,T) >_\tau /U_0$ and c) standard deviation over the T_τ time window $std(V_\theta(r,\theta,T))/U_0$ for the right vortex ($U_0 = 5\ m/s$; $\alpha = 3^o$), $T = 22$.

From each sliding time-average velocity field, an azimuthal average in the θ-wise direction is further performed to produce a $< V_\theta(r,T) >_{\tau,\theta}$ vortex velocity profile :

$$< V_\theta(r,T) >_{\tau,\theta} = \frac{1}{N_\theta} \sum_{i=1}^{N_\theta} < V_\theta(r,\theta_i,T) >_\tau \tag{7}$$

where N_θ is the angular resolution of $< V_\theta >_\tau$ and $r \in [0 : r_{max}]$. Thereafter we use the notation $< X >_{\tau,\theta}$ to refer to this azimuthal averaging. The resulting data is finally averaged over the N different realizations which were repeated, yielding

$$\overline{V_\theta}(r,T) = \frac{1}{N} \sum_{i=1}^{N} (< V_\theta(r,T) >_{\tau,\theta})_i \tag{8}$$

The average velocity profiles $\overline{V_x}$, $\overline{V_\theta}$ and $\overline{V_r}$ are shown in Fig.12 for $T = 22$ with the dispersion of the results that stems from the $N = 4$ realizations. This dispersion is weak outside of the core region. The larger dispersion of velocity data inside the core is associated to velocity gradients in this region. The dispersion on the axial $\overline{V_x}$ profiles is caused in part by the misalignment between the V_θ field and the out-of-plane V_x field shown in Fig. 7. However, one can observe that the average velocity $\overline{V_\theta}$ and $\overline{V_r}$ effectively drops to 0 at $r \to 0$, which confirms the good precision on the detection of the centroid.

The question of the fit of the vortex profile against analytical models is of interest for the full description of the flow and the applicability of fundamental results known generally for these models. Numerical fits are performed considering the Batchelor model [17] yielding good results. In general, the Batchelor profile slightly under-estimates the vortex circulation and over-estimates the core size. The axial velocity profile is not well represented by the Gaussian evolution, however, the peak values of $\overline{V_x}^B$ follow the same time evolution as $\overline{V_x}$ and are therefore considered sufficient for the purposes of this work.

An estimation of the error between the averaged vortex profile $\overline{V_\theta}(r,T)$ and the real azimuth-averaged profile $V_\theta(r,T)$ is obtained by applying the aforementioned procedure into a dipole of Batchelor vortices. Two Batchelor vortex fields of circulation and radius similar to that of the experimental data were cast into the SPIV mesh-grid. An position uncertainty in the order of the SPIV grid step was added to the artificial vortex centroid. It was found that the interpolation and averaging steps described above introduced a maximum error of 0.25% of the peak azimuthal velocity which is negligible for the purposes of this work.

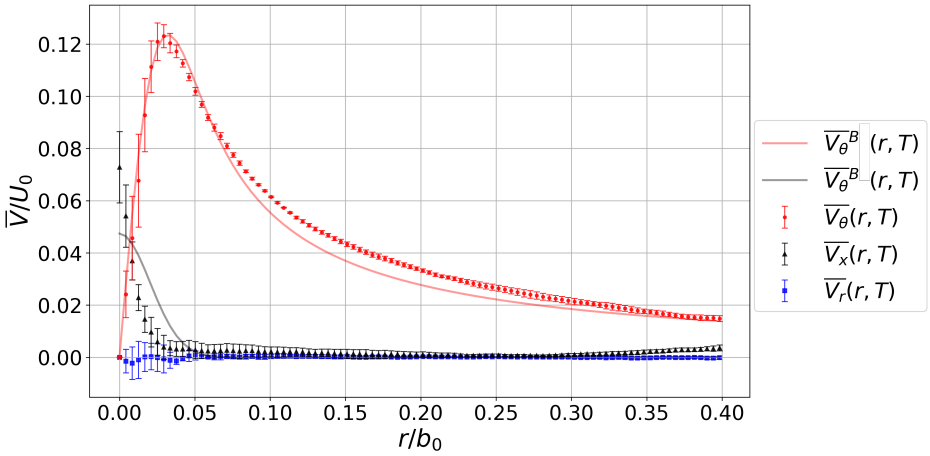

Fig. 12 Average vortex velocity profile $\overline{V_\theta}/U_0$, $\overline{V_x}/U_0$ and $\overline{V_r}/U_0$ and Batchelor vortex fit results (superscript B). at $T = 22$ for the reference wing towed at $U_0 = 5$ m/s and $\alpha = 3^o$. Dispersion between runs is represented by error bars.

5. Averaged vortex characterization

To proceed further with the characterization of the vortex requires the radial vorticity profile $\overline{\omega}_x(r,T)$. The average procedure (equations 6, 7 and 8) is applied yielding :

$$\overline{\omega_x}(r,T) = \frac{1}{r}\left[\frac{d}{dr}\left(r\overline{V_\theta}(r,T)\right)\right] \tag{9}$$

The evolution of $\overline{\omega}_x(r,T)$ as a function of r is plotted in Fig.13a for a representative time, $T = 27$. It shows that the vortex is a compact structure with $\overline{\omega}_x(r,T)$ concentrated in the region of small r. The approximate size of which can be taken as the radius R_ω defined by

$$\overline{\omega}_x(r = R_\omega) = c_\omega \max(\overline{\omega}_x(r)) \tag{10}$$

where $c_\omega = 1\%$ is a value corresponding to the resolution on ω_x provided by the SPIV data. This means that all the vorticity is contained in the region $r \leq R_\omega$ and that beyond $r > R_\omega$ measurements are in the order of magnitude of the noise.

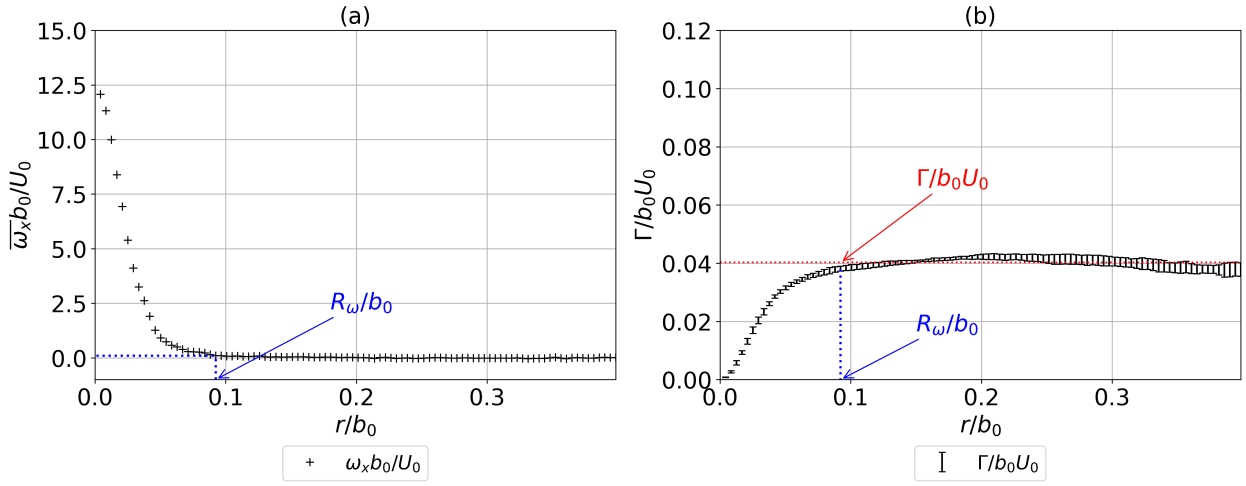

Fig. 13 a) Non-dimensional vorticity $\overline{\omega_x}(r,T)$ and b) non-dimensional circulation $\Gamma(r,T)/b_0U_0$, for vortices trailing behind the reference wing configuration at $T = 35$. The radial distance R_ω is shown in blue and the vortex total circulation Γ is shown in red.

The circulation of the vortex is obtained by considering the azimuthal velocity field following

$$\Gamma(r,T) = 2\pi r\overline{V_\theta}(r,T) \tag{11}$$

The evolution of $\Gamma(r,T)$ as a function of the radial distance is plotted in Fig.13b for $T = 35$. The vortex total circulation $\Gamma(T)$ is obtained from averaging $\Gamma(r,T)$ in the region outside the vortex core [46] that is from $r = R_\omega$ to $r_{max} = 0.4b_0$.

$$\Gamma(T) = \frac{1}{b/2 - R_\omega}\int_{R_\omega}^{b/2}\Gamma(r,T)dr \tag{12}$$

This methodology to evaluate $\Gamma(T)$ allows to cope with situations when no clear asymptotic value is found in the $\Gamma(r,T)$ evolution as a function or r, as it is often the case in the present dataset. Furthermore, the vortex circulation can also be deduced from the generated lift (considering an elliptic loading model) :

$$\Gamma = \frac{F_z}{\frac{\pi}{4}b_0\rho U_0} \tag{13}$$

For most experiments, the circulation value deduced from the lift measurements is slightly stronger than that measured through SPIV. On one hand, this is related to the higher vortex separation b observed in practice and on the other hand to possible loss or addition of vorticity during towing caused by the experimental installation (the wake of the strut).

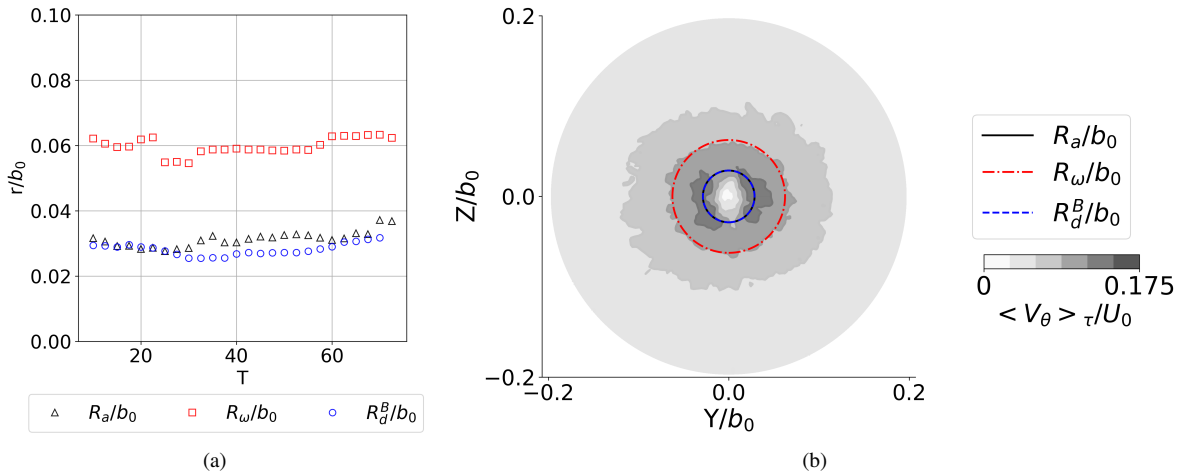

(a) (b)

Fig. 14 Core size $R_a(T)$, dispersion radius $R_d^B(T)$ and radial distance in which the vorticity is contained R_ω for a vortex trailing behind the reference configuration : a) time-evolution and b) illustration on a 2D vortex field at $T = 22$.

The second property of interest is the vortex radius. We introduce first the vortex core size $R_a(T)$ as

$$\overline{V_\theta}(r = R_a, T) = \max(\overline{V_\theta}(r,T)). \tag{14}$$

Which is computed using a cubic interpolation scheme on the discrete grid of the SPIV set. The dispersion radius R_d is further used. It is defined as:

$$R_d^2 = \frac{1}{\Gamma_0}\int_\Omega r^2\overline{\omega}(r)d\Omega \tag{15}$$

Eq. 15 is sensitive to measurement noise in the external region of the vortex, which is common in the present dataset. Indeed, for $r > R_\omega$ vorticity values are in the same order of magnitude as noise. Let $\overline{\omega}^B(r)$ be a Batchelor vorticity profile [17] fitted into the experimental data. The dispersion radius is therefore estimated by R_d^B, for which $\overline{\omega}^B(r)$ has been input into equation 15. The evolution of R_a, R_ω and R_d^B is plotted as a function of time in Fig. 14a. The order of

magnitude of R_a is close to values reported in other experimental studies [16]. At $T = 22$, it is found that the estimated dispersion radius R_d^B is slightly smaller than the core size R_a (the curves superpose in Fig.14b). At the same instant R_ω is larger than R_a by a factor of ≈ 2.18. The hierarchy of these different evaluations of the vortex size is conserved during the entire evolution of the flow (see Fig.14a). An illustration of the order of magnitude of the radii with respect to the vortex field is shown for $T = 22$ in Fig. 14b.

B. Effect of the flow parameters

In this section, the evolution of vortex characteristics as a function of towing velocity U_0 and angle of attack α for the reference wing configuration is described. Wake vortices characteristics as well as the aerodynamic forces generated by the towed reference wing are compared for experiments on a range of $U_0 \in [1\ m/s : 5\ m/s]$ and $\alpha \in [0^o : 5^o]$.

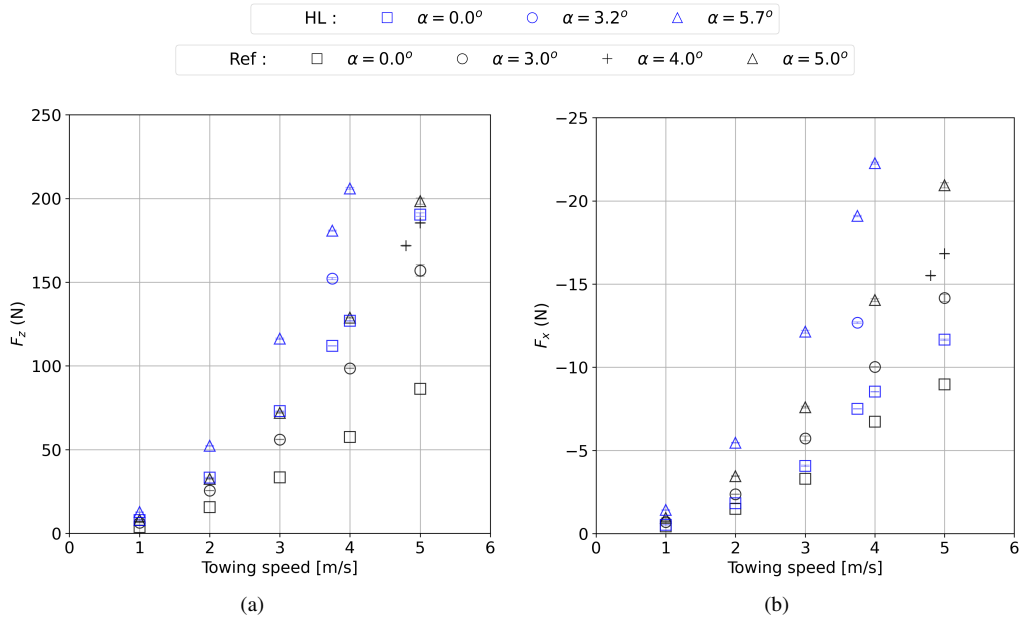

(a) (b)

Fig. 15 Total a) lift and b) drag measurements generated by the reference wing as a function of angle of attack α and towing velocity of U_0.

A comparison of the dynamics of a vortex trailing behind the same aircraft under cruise and landing configurations will be presented in sec. III.C. Experiments will be compared at equal aerodynamic load, since an equal mass must be lifted in both flight configurations. This is why, instead of analyzing the aerodynamic coefficients C_z and C_x as it is custom, the evolution of aerodynamic lift F_z and drag F_x generated by the reference and high-lift wings as a function of towing velocity and angle of attack is shown in Fig. 15. The results for the high-lift configuration will be commented in sec. III.C. The dispersion on the lift and drag mean values is on the order of 3% at maximum.The increase of drag and lift forces with angle of attack and with the square of towing velocity is expected.

The evolution of vortex characteristics as as function of U_0 and α are shown in Fig. 16. These characteristics are computed in the mid-field, at a downstream station of 30 wing-spans behind the wing. The evolution of non-dimensional circulation Γ/b_0U_0 is shown in Fig.16a. The dispersion in Γ between repetitions of the same experiment is in the order of 2.75%. Due to time constraints, for $\alpha = 0^o$, experiments were realized once. As expected, a clear linear increase with angle of attack is seen for the circulation measurements. A linear interpolation of the $U_0 = 5\ m/s$ data yields, for α in degrees, $\frac{\Gamma}{b_0U_0}(\alpha) = 0.006\alpha + 0.022$ with a mean square error of 2×10^{-6}. This behavior is coherent with lifting line theory and it is justified as more lift is produced with increasing angle of attack (see Fig. 15a). As expected, non-dimensional circulation values are independent of the towing velocity, confirming a linear relationship between circulation and towing velocity U_0. A relatively high value of $\frac{\Gamma}{b_0U_0}$ is observed for $U_0 = 2$ m/s, $\alpha = 0^o$, which could not be explained.

The evolution of non-dimensional core sizes R_a/b_0 and R_ω/b_0 at $T = 30$ as a function of U_0 and α is shown in Fig.

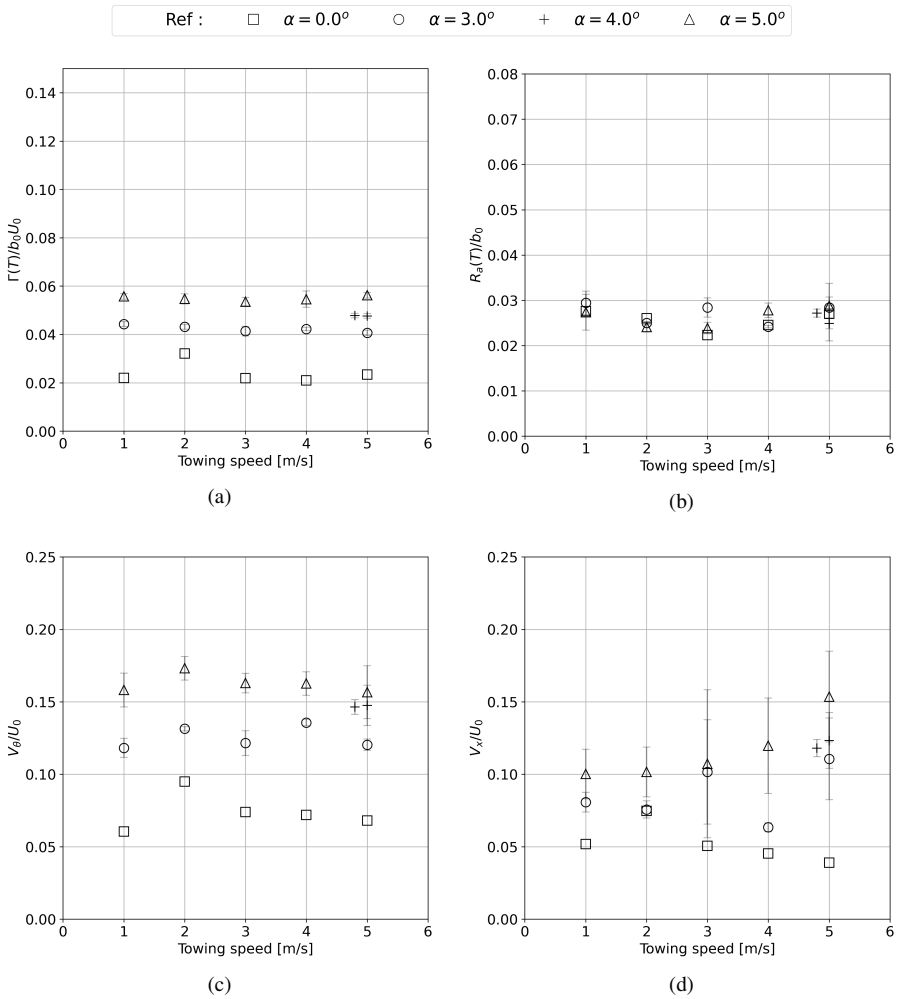

Fig. 16 a) Non-dimensional circulation, b) core size c) peak azimuthal velocity and d) peak axial velocity as a function of towing velocity U_0 and angle of attack α for the right vortex trailing 30 wing-spans downstream of the reference wing.

16b. The values of R_a are in the same order of magnitude as values reported in the literature [27]. No significant change in R_a/b_0 is observed over the range of flow parameters studied. Namely, the magnitude of the measured vortex core size remained independent of the generated lift. The evolution of the external radius indicator R_w mirrors that of R_a and its magnitude is on the order of $2R_a$ as it will be shown further below.

At $T = 30$, the evolution of $\overline{V_{\theta max}}/U_0$ mirrors that of the circulation, as they both have the same dependency on the generated lift (see Fig. 16c). This also relates to the independence of R_a from U_0 and α. Peak axial velocity $\overline{V_{xmax}}/U_0$, however, exhibits an evolution that is dependent of both U_0 and α (see Fig. 16d). For $\alpha = 0^o$, less dimensionless axial velocity is generated at increasing towing velocity. At $\alpha = 5^o$, more dimensionless axial velocity is generated at increasing towing velocity. For all configurations at $T = 30$, axial velocity is on the same order of magnitude as azimuthal velocity and it is oriented towards the wing (wake flow). $\overline{V_{xmax}}$ equals $\overline{V_{\theta max}}$ for the highest absolute azimuthal velocities considered, at $\alpha = 5^o$ and $U_0 = 5$ m/s.

We use the axial flow parameter, or swirl number q to measure the ratio of azimuthal to axial velocities in the vortex.

$$q = \frac{\Gamma}{2\pi R_d \Delta U} \tag{16}$$

Where ΔU is the difference between far-field velocity ($r \to \infty$) and the maximum axial flow in the core of the vortex, here $\Delta U = \overline{V_{xmax}}$. As stated above, the parameter q is used in analytical and numerical works to study the linear stability of the Batchelor vortex. q values shown in this work are therefore obtained through a fit of the Batchelor model into the experimental data yielding $q = \frac{\Gamma^B}{2\pi R_d^B \Delta U^B}$. Furthermore the values $0 < q < 1.5$ are considered as a configuration

that promotes the development of modes of helical instabilities in the vortex (see Delbende *et.al* [23], Olendraru *et.Al* [24] and Jacquin & Pantano [47]). The evolution of q as a function of U_0 and α at $T = 30$ is summarized in table 3. In the experiments of this work, q is dependent on the angle of attack α and on the towing velocity U_0. The former is expected from eq.16. The later is related to the evolution of $\overline{V_{x}}_{max}$ described above. At $T = 30$, none of the U_0-α configurations reaches an unstable swirl number value.

U_0 **(m/s)**	1.0	5.0
$\alpha = 0^o$	1.82	2.75
$\alpha = 3^o$	2.29	1.71
$\alpha = 5^o$	2.48	1.61

Table 3 Swirl number q at $T = 30$ as a function of angle of attack α and towing velocity U_0 for the right side vortex trailing behind the reference wing

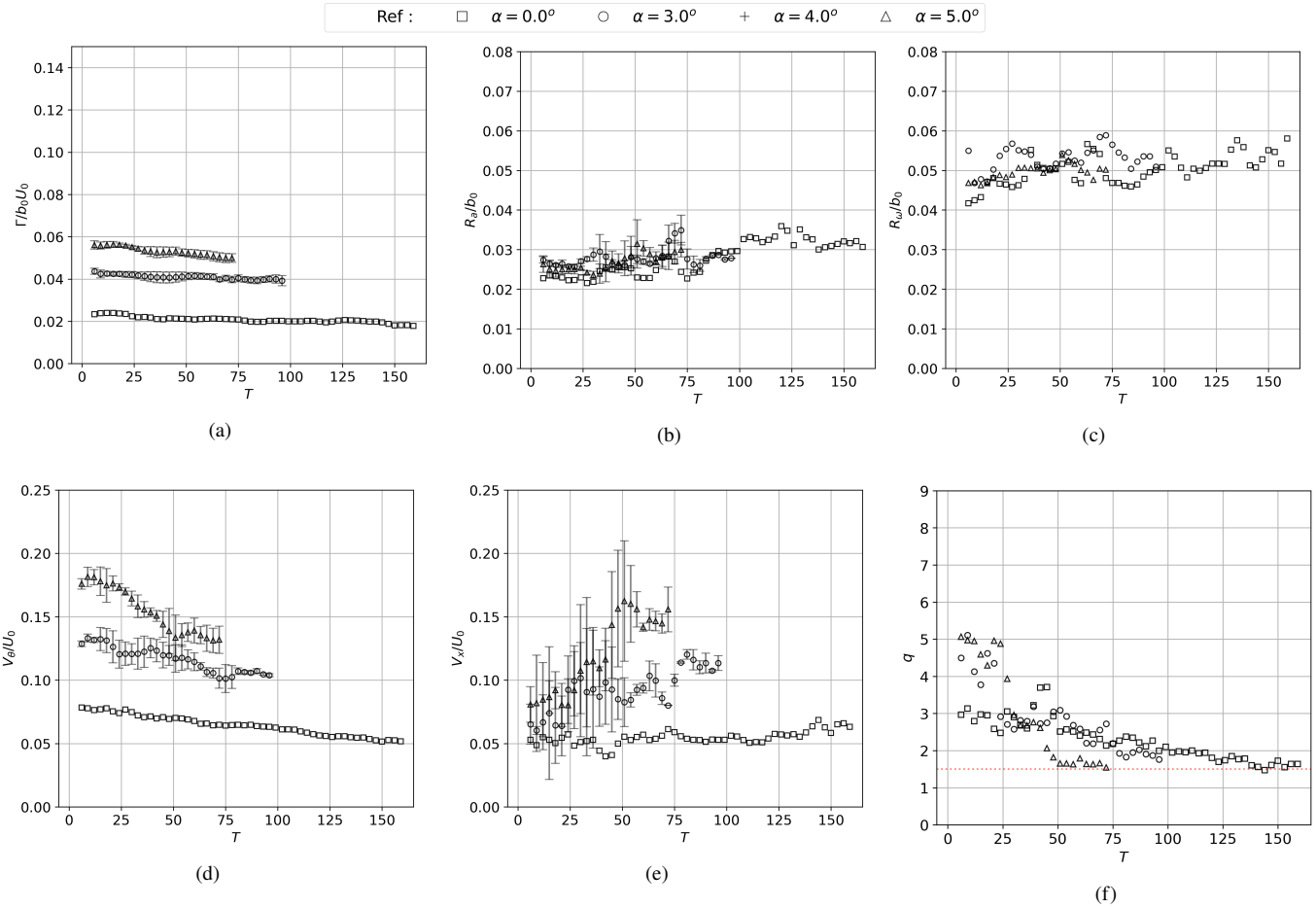

Fig. 17 Non-dimensional a) circulation, b) core size, c) vorticity scale, d) peak azimuthal velocity, e) peak axial velocity and f) swirl number (from a fitted Batchelor vortex) as a function of time for the right side vortex trailing downstream of the reference wing at a towing velocity of $U_0 = 3m/s$.

For $U_0 = 3$ m/s, the time evolution of dimensionless Γ, R_a, R_ω $\overline{V_\theta}_{max}$, $\overline{V_x}_{max}$ and q is shown in Figs. 17a, b, c, d, e and f respectively. Time is considered in terms of downstream evolution T. Error bars represent the dispersion between repetitions of an experiment. Let $\Delta X(T)/\Delta T$ be the linear rate of evolution of a given variable X corresponding to the slope of a linear regression performed on $X(T)$. A linear decrease is observed in the evolution of circulation ($\Delta\Gamma/\Delta T < 0$, see Fig. 17a) and maximum azimuthal velocity ($\Delta\overline{V_\theta}_{max}/\Delta T < 0$, see Fig. 17d). The slope of the

decrease is greater when increasing the angle of attack. This behavior is explained by the viscous diffusion which acts on the vortices and increases with the velocity in the vortex field. A similar linear increase is observed in the evolution of core sizes R_a (see Fig. 17b), however, the value $R_a(T)$ and rate of increase $\Delta R_a/\Delta T$ are not dependent of the angle of attack. The rate of increase $\Delta R_a/\Delta T$ shown in Fig. 17b is in close agreement with the rate of increase of viscous diffusion for a Lamb-Oseen vortex core. For the complete duration of the experiment, the behavior of R_a is mirrored by that of R_ω (see Fig. 17c) and $R_\omega \approx 2R_a$. The diffusion of the vortex is translated in the external region ($r > R_\omega$) by the decrease of Γ and increase of R_ω, and in the core region by the increase of R_a [18]. The rate of decrease of peak azimuthal velocity $\Delta\overline{V_\theta}_{max}/\Delta T$ is in an order of magnitude superior to that of the circulation, suggesting that another phenomenon is acting on top of viscous diffusion. A decrease of azimuthal velocity at quasi-constant circulation has been related to the action of pressure perturbations in the vortex core [19]. The pressure differential in the core can in turn be related to the axial velocity in this region. Wake type axial velocity increases weakly over the considered time window for $\alpha = 0^o$ and sees a sharp increase over time for $\alpha = 3^o$ and 5^o (see Fig. 17e). For $\alpha = 3^o$ and 5^o, the time evolution of $\overline{V_x}_{max}$ seems to become non-monotonous right before the exit of the vortex from the measurement window. Similarly to the case of Γ and $\overline{V_\theta}_{max}$ the slope of evolution of peak axial velocity $\Delta\overline{V_x}_{max}/\Delta T$ seems proportional to the angle of attack. An increase of axial velocity can be explained by the diffusion of azimuthal velocity since centrifugal forces generated by V_θ decrease, thus increasing the pressure drop at the vortex axis [17]. Furthermore, for $U_0 = 3$ m/s, at $\alpha = 0^o$, $\Delta\overline{V_x}_{max} < \Delta\overline{V_\theta}_{max}$, where as for $\alpha = 3^o$ and $\alpha = 5^o$ $\Delta\overline{V_x}_{max} > \Delta\overline{V_\theta}_{max}$. Therefore, the increase of axial velocity towards the wing seems to be governed by two parameters, namely the rate of azimuthal velocity decrease (initiated by viscous diffusion) and the pressure drop in the core of the vortex (related to the flow conditions around the wing). The swirl number q seems to decrease monotonically over time until the threshold 1.5 is reached. This threshold is shown by a red line in Fig. 17f. Namely, for the experiment at $U_0 = 3$ m/s, $\alpha = 5^o$ shown in Fig. 17f, q decreases sharply until $T = 50$ at which $q = 1.5$ is reached. For $T > 30$, the value of q remains constant. The stagnation of q is translated in the behavior of $\overline{V_\theta}_{max}$ and $\overline{V_x}_{max}$. As stated above, $q < 1.5$ is a region of instability for the Batchelor vortex. The resistance of the vortex to destabilization from axial velocity has been observed in analytical and DNS works [48], [47].

A linear regression is performed over the time evolution data of vortex characteristics for $U_0 \in [1; 5]$ m/s and $\alpha \in [0; 5]^o$. The slopes obtained by this method are provided in Fig. 18. The behavior described above for $U_0 = 3$ m/s is observed for almost all configurations except for the $\alpha = 4^o$ data for which an outlier behavior is observed. Close inspection of the $U_0 = 4.8$ m/s, $\alpha = 4^o$ data (not shown) reveals a particularly unsteady behavior and a quick exit from the SPIV window, both of which hurdle the linear regression procedure. A stronger rate of decay of circulation and azimuthal velocity is obtained when increasing α (see Figs. 18a and 18c). With increasing towing velocity, $\Delta\Gamma/\Delta T$ is conserved, but the absolute value of $\Delta\overline{V_\theta}_{max}/\Delta T$ is decreased. A stronger rate of increase of axial velocity is obtained when increasing α, (except for the $U_0 = 4.8$ m/s, $\alpha = 4^o$ data), see Fig. 18d. $\Delta\overline{V_x}_{max}/\Delta T$ increases with U_0 with the exception of the experiments $U_0 = 4$ m/s, $\alpha = 5^o$ and $U_0 = 5$ m/s, $\alpha = 5^o$. The evolution of $\overline{V_x}_{max}$ in these cases is not monotonous, as it will be further shown on the following. The expansion of the vortex, translated by the growth of core size $\Delta R_a/\Delta T$ (see Fig. 18b), seems independent of α, but slows down with increasing towing velocity (except for the $\alpha = 4^o$ data). This behavior is mirrored by $\frac{\Delta R_\omega}{\Delta_T}$ and $\frac{\Delta R_d^B}{\Delta_T}$ (not shown). On all configurations, the order of magnitude of $\Delta\Gamma/\Delta T$ and $\Delta R_a/\Delta T$ is $O(10^{-4})$ and for $\Delta\overline{V_\theta}_{max}/\Delta T$ and $\Delta\overline{V_x}_{max}/\Delta T$ it is $O(10^{-3})$, which corroborates that the decrease of $\overline{V_\theta}_{max}$ is linked to the development of $\overline{V_x}_{max}$ rather than to viscous diffusion.

C. Effect of the wing load profile

The comparison of the vortex characteristics between the reference (cruise flight) and high-lift configurations is looked upon. The evolution of aerodynamic lift F_z and drag F_x generated by the high-lift wing is shown as a function of towing velocity and angle of attack in Fig. 15. Similar to the results for the reference configuration, the dispersion on the lift and drag mean values is on the order of 3% at maximum. The high-lift and reference wing models feature the same planform area and airfoil profile but a different span-wise loading profile so they were expected to exhibit different lift forces under the same U_0 and α towing configuration. Namely, the high-lift wing generates more lift while maintaining drag values close to the reference wing at equal towing speed and angle of attack. For example, the same lift of $\sim 155N$ is generated at iso-α with a reduction of 25% of velocity.

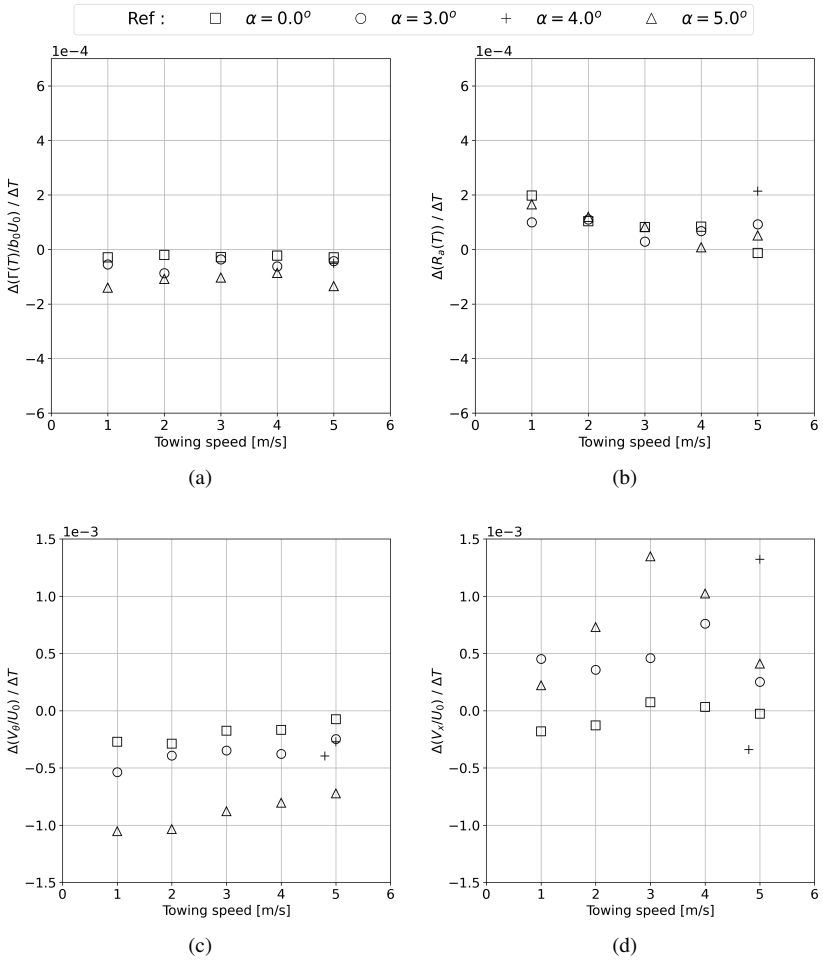

Fig. 18 Linear rate of evolution a) Non-dimensional circulation, b) core size, c) peak of azimuthal velocity and d) peak of axial velocity as a function of angle of attack α for the right side vortex trailing 25 wing-spans downstream of the reference wing at a towing velocity of $U_0 = 5m/s$.

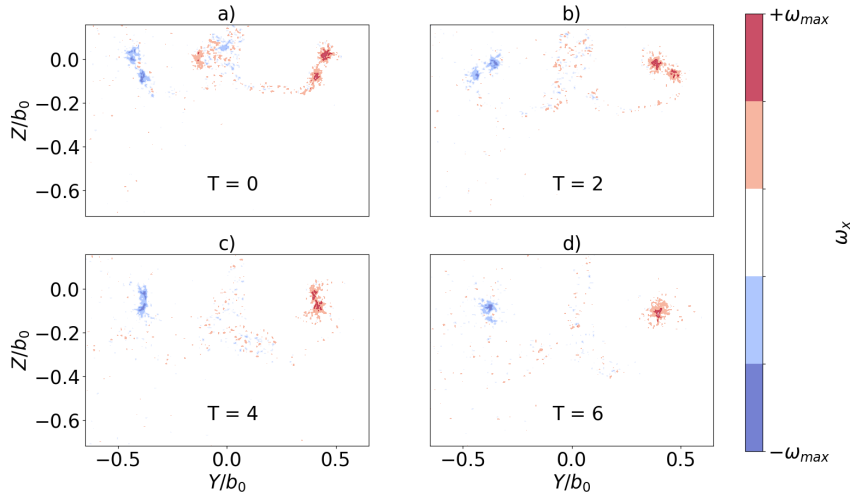

Fig. 19 Axial vorticity magnitude ω_x on the wake of the high-lift wing configuration towed at $U_0 = 2$ m/s and $\alpha = 0^o$. Elapsed non-dimensional time T, corresponding to different downstream locations are represented.

As stated in section II.A, the span-wise evolution of geometrical twist in the high-lift wing is discontinuous at $y = 0.375b_0$ from the wing plane of symmetry. Secondary vorticity is shed from the "flaps" as it would be expected based on theoretical [49] and experimental [10], [13] documentation. Fig.19 shows the flow field measured after towing the high-lift wing at 4 successive time instants and indicates the typical vorticity distribution observed. Besides the main vorticity structure shed from the wing tips with a magnitude Γ_1, a secondary structure of same sign and lower magnitude Γ_2 is observed in the near-wake. At $T \approx 0$, this secondary vortex is located trailing near the wing flaps, see Fig.19.a. On subsequent measurements, the secondary structure is transported in an orbital trajectory around the wing-tip vortex until both vortices fuse, around $T \approx 6$, see Fig.19.d. This behavior of co-rotating wake vortices is consistent with other experimental results [10].

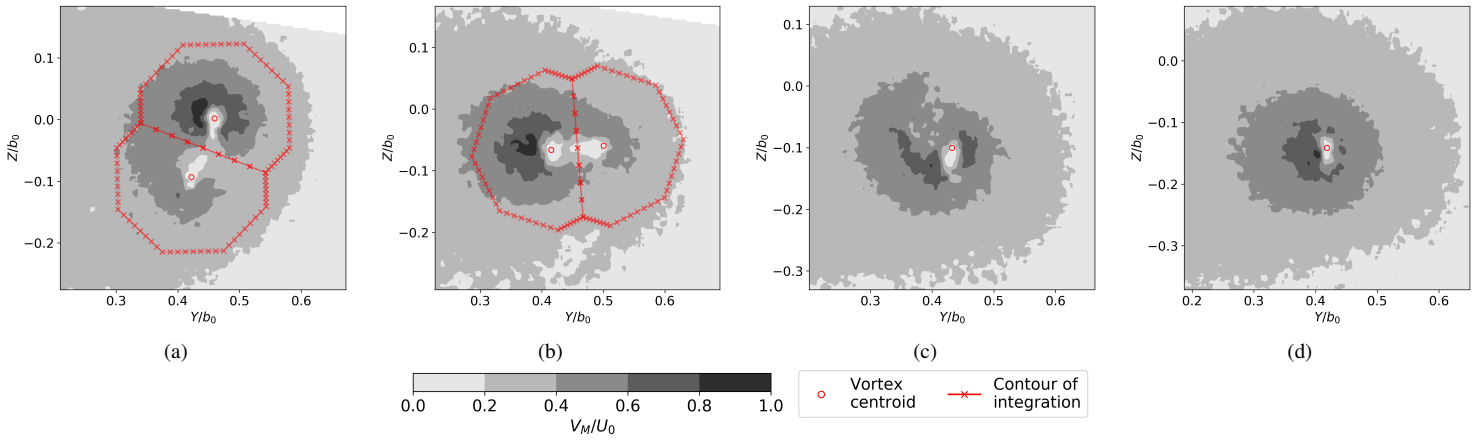

Fig. 20 Right side of the vortex wake generated by the high lift wing at $\alpha = 5.7^o$ and $U_0 = 3.75$ m/s at a) $T = 1.5$, b) $T = 3.0$, c) $T = 4.5$ and d) $T = 6.0$. The contours to measure the vortices circulation are displayed when two vortices are detected in the wake.

Let $r_\Gamma = \Gamma_2/\Gamma_1$ be the ratio of circulation between the right side vortex shed by the flap and the one shed by the wingtip. $b_r = b_2/b_1 = 0.75$ is the ratio of distances between the flap tips and the wing tips from which vorticity is shed. Four subsequent snapshots of the right side of the vortex wake generated by the high lift wing towed at $U_0 = 3.75$ m/s and $\alpha = 5.7^o$ are shown in Fig. 20. At $\Delta t = 0.2s$, each snapshot is separated by a dimensionless time $\Delta T = 1.5$ representative of 1.5 wingspans downstream on the wake. The fusion of the two vortical structures can be observed as the velocity field transits from being distributed in two clear lobes (see Fig. 20a) to an axisymmetric distribution around a single center (see Fig. 20d). Let $\overrightarrow{x}_{\Gamma 1,1}$ be the center of the wingtip vortex and $\overrightarrow{x}_{\Gamma 1,2}$ that of the flap vortex defined by the $\Gamma 1$ criterion. To detect the presence of secondary vorticity $\overrightarrow{x}_{\Gamma 1,2}$, we define each vortex as a compact region of $\Gamma 1(\overrightarrow{x}) > 0.75$ (not shown in Fig. 20). This threshold methodology allows for the detection of the end of the fusion phase, as an unique compact region of $\Gamma 1(\overrightarrow{x}) = 0.75$ is detected, see Figs.20c and 20d. When secondary vorticity is detected, the ratio of circulation is computed by integrating the velocity field over polygonal contours centered around $\overrightarrow{x}_{\Gamma 1,1}$ and $\overrightarrow{x}_{\Gamma 1,2}$. The limit between integration contours is the mediatrix of the segment defined by ($\overrightarrow{x}_{\Gamma 1,1}$ - $\overrightarrow{x}_{\Gamma 1,2}$). The circulations Γ_1 and Γ_2 resulting from each integration are compared to define r_Γ.

$r_\Gamma(T)$ is computed for each repetition of a towing experiment, yielding a dispersion between repetitions in the order of ± 0.05. Let $\overline{r_\Gamma}$ be the phase average of the repetitions of an experiment (see eq.8). $\overline{r_\Gamma}$ right after the passage of the high lift wing ($T \sim 1$) as a function of angle of attack and towing velocity is shown in Fig. 21a. The ratio of circulation is weakly dependent of U_0 and decreases with α in a seemingly linear rate. At $\alpha = 0^o$, both vortices have similar strength. For $\alpha = 5.7^o$, the strength of the flap vortex is approximately 0.6 times that of the wingtip vortex. For all configurations studied, the rate of decrease over time of $\overline{r_\Gamma}(T)$ is also independent of towing velocity U_0 (not shown). This behavior is expected from the circulation results of the reference wing presented in section III.B (see Fig. 16a). Vortex fusion time is dependent of the initial distance between the vortices b_r and on their strength ratio r_Γ [10]. As expected, fusion time shortens from $T \sim 6$ for experiments at low angle of attack to $T \sim 4$ at high angle of attack. Fusion time values are in agreement with those reported in a similar experiment in a wind tunnel [16].

The average velocity profiles for the vortex trailing 26 wingspans downstream of the high-lift configuration are

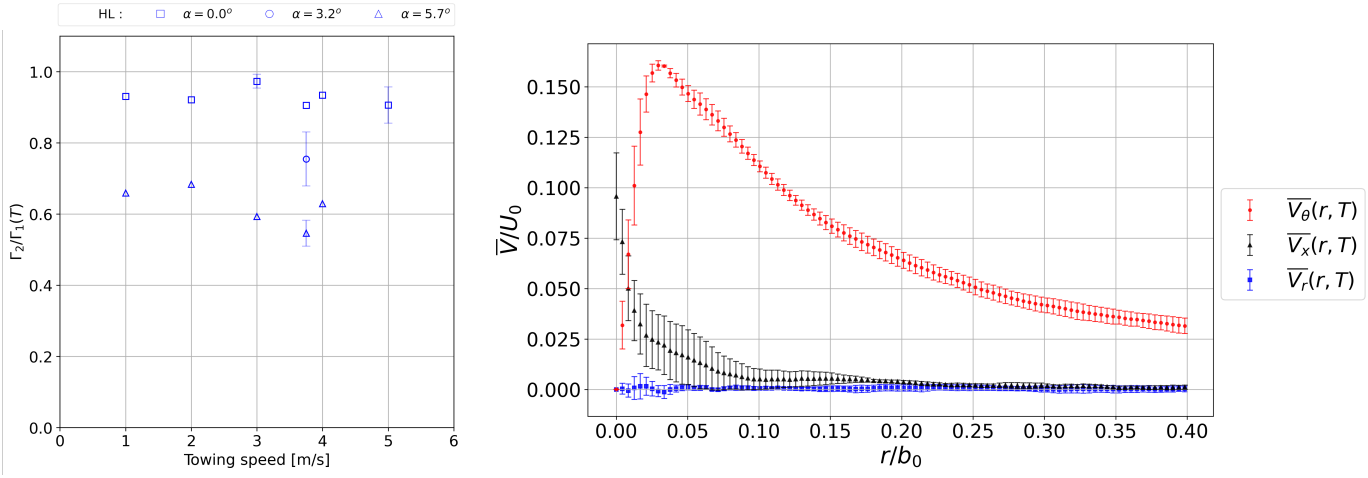

(a) (b)

Fig. 21 a) Measured ratio of circulation $\overline{r_\Gamma}(T \sim 1)$ (when two vortices are detected in the right side of the wake of the high lift wing) as a function of angle of attack α and towing velocity U_0. b) Averaged vortex velocity profile $\overline{V_\theta}$, $\overline{V_x}$ and $\overline{V_r}$ at $T = 26.3$ for the high-lift wing towed at $U_0 = 3.75$ m/s and $\alpha = 3.2^o$. Dispersion between runs is represented by error bars.

shown in Fig. 21b. The "post-fusion" $\overline{V_\theta}$ and $\overline{V_x}$ profile differs from a Gaussian profile in a region approximately delimited by $[R_a; R_\omega]$. In this region $\overline{V_\theta}$ decreases at a seemingly constant rate. The vortex profile is not Gaussian, as it has been reported by similar studies [20],[5] and [16].

To further compare the wakes trailing behind wings of different loading profiles, the total lift force generated by each wing must be equal. Changes in the strength, structure and timescales of the vortices can then be related to the evolution of ℓ_y. Configurations for which F_z^{HL} and F_z^{Ref} are considered close enough for a comparative analysis are provided in table 4. It is noteworthy that the lift curve the high-lift wing at $\alpha = 0^o$ blends with that of the reference wing at $\alpha = 5^o$ (see Fig. 15a) yielding also a comparison at iso-C_Z. The main results in terms of circulation and core size evolution are summarized in this table and commented on on the following.

F_z (N)	8	32 ± 1	72 ± 1	128 ± 1	155 ± 2	198 ± 8	198 ± 8
***Ref* wing**	1m/s, 5^o	2m/s, 5^o	3m/s, 5^o	4m/s, 5^o	5m/s, 3^o	5m/s, 5^o	5m/s, 5^o
***HL* wing**	1m/s, 0^o	2m/s, 0^o	3m/s, 0^o	4m/s, 0^o	3.75m/s, 3.2^o	4m/s, 5.7^o	5m/s, 0^o
Γ^{HL}/Γ^{Ref}	1.08	1.16	1.20	1.19	1.46	1.30	1.16
R_a^{HL}/R_a^{Ref}	1.27	1.51	1.55	1.50	1.13	1.63	1.97

Table 4 Towing configurations, noted as (U_0, α) for which the reference and high-lift wings generate comparable lift as shown in Fig. 15. Circulation and core size ratios between configurations are shown.

Consider the case of $F_z \sim 155N$ for which both wings are towed at a similar angle of attack. The time evolution of non-dimensional circulation for these two experiments is provided in Fig. 22a. In the case of the high-lift wing, only the "post-fusion" data is shown. Following the decrease in velocity, circulation is increased on the high-lift configuration as it is expected from eq. 13. However, the measured increase of circulation $\Gamma^{HL}/\Gamma^{Ref} \approx 1.5$ is 9% higher than that predicted by the ratio of towing velocities $U_0^{Ref}/U_0^{HL} = 4/3$. Vortex separation is not equal between the configurations, which explains the under-estimation of the model. The maximum cross flow velocities $\overline{V_\theta}$ obtained for $\alpha = 5^o$ range in 0.2 of freestream velocity in agreement with other experimental results [16].

The evolution of non dimensional circulation as a function of U_0 and α at $T = 30$ is shown in Fig. 22b. At equal towing velocity and angle of attack, vortices generated by the high-lift wing see a clear increase of Γ/b_0U_0 with respect to those generated by the reference configuration (see Fig. 16a). A large dispersion of data is observed for Γ at $U_0 = 1m/s, \alpha = 5^o$, the reasons for which are unknown. Upon comparison with Fig. 16a, it can be seen that for all

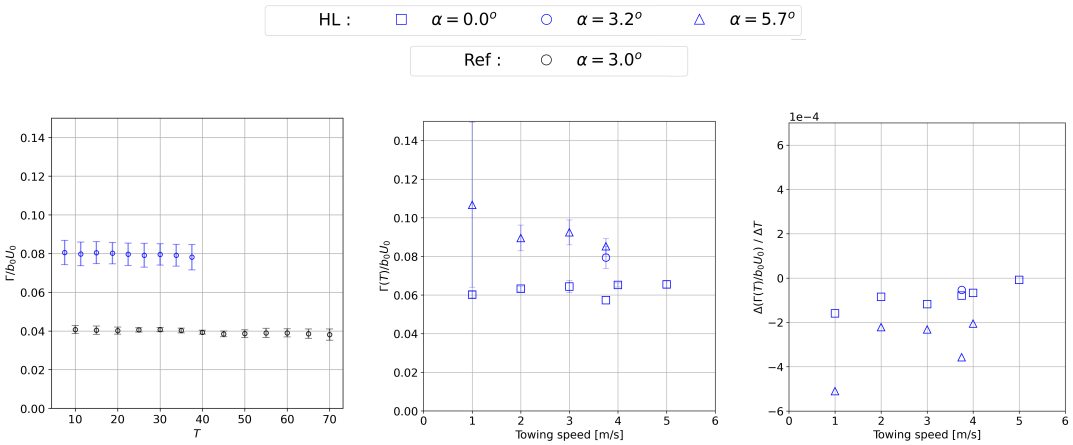

(a) (b) (c)

Fig. 22 Non dimensional circulation for a vortex generated by the high-lift configuration : a) Comparison of the high-lift wing vortices ($U_0 = 3.75m/s, \alpha = 3.2^o$) with respect to the reference wing vortices ($U_0 = 5m/s, \alpha = 3^o$) at iso-total lift of $155N$ and as a function of time, b) circulation as a function of U_0 and α for $T = 30$, c) linear rate of evolution as a function of U_0 and α.

configurations at iso-total lift the ratio of measured circulations is higher than that predicted by eq. 13.

Finally, the linear evolution rate of circulation $\Delta\Gamma/\Delta T$ for the high-lift wing as a function of towing velocity and angle of attack is shown in Fig. 22c. Under equal towing conditions, the circulation of the high-lift vortices decrease at a stronger rate than those generated by the plain rectangular wing (see Fig. 18a). This is expected from the increase in cross-flow velocity. There is, however, an acceleration of circulation decay with lower towing velocity, which was not the case for the reference wings. At iso-total generated lift, the rate of decay of circulation is equal between both wing configurations with the exception of the pair *Ref*: $U_0 = 5m/s, \alpha = 5^o$ and *HL*: $U_0 = 5m/s, \alpha = 0^o$. The circulation for *HL*: $U_0 = 5m/s, \alpha = 0^o$ is particularly persistent over time. The vortex quickly descends until the end of the measurement window, making impossible the computation of the rate of circulation decay.

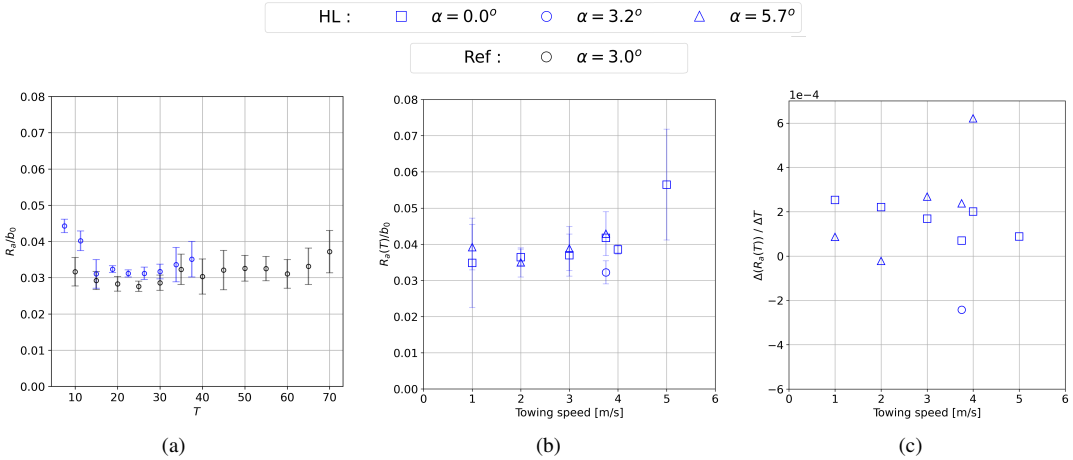

(a) (b) (c)

Fig. 23 Non dimensional core size for a vortex generated by the high-lift configuration : a) Comparison of the high-lift wing vortices ($U_0 = 3.75m/s, \alpha = 3.2^o$) with respect to the reference wing vortices ($U_0 = 5m/s, \alpha = 3^o$) at iso-total lift of $155N$ and as a function of time, b) R_a/b_0 as a function of U_0 and α for $T = 30$, c) linear rate of evolution as a function of U_0 and α.

The time evolution of non-dimensional core size at iso-total lift $F_z = 155N$ is provided in Fig. 23a. The measured core size sees an initial decrease from the end of the fusion phase ($T \sim 6$) to the end of the extended near-field $T = 15$. This is thought to be related to the remnants of the fusion and roll-up process. Here, vorticity is still being engulfed into the vortex, increasing its peak azimuthal velocity and tightening the core size over time. Besides this configuration, this

phenomenon is observed in the high lift wing only for $U_0 = 2m/s, \alpha = 5.7^o$. At $T = 30$, the core size is enlarged by a factor of $\frac{R_a^{HL}}{R_a^{Ref}} \approx 1.1$ with respect to the reference wing vortex in Fig. 23a. The evolution of R_a/b_0 as a function of U_0 and α at $T = 30$ is shown in Fig. 23b. For all configurations, vortices generated by the high-lift wing have a slightly larger core size R_a than the reference. $\Delta R_a/\Delta T$ for the high-lift wing as a function of towing velocity and angle of attack is shown in Fig. 23c. For $\alpha = 0^o$, the widening of R_a is decelerated with increasing towing velocity, as observed for the reference wing in Fig. 18b. However, for $\alpha = 5.7^o$ the opposite behavior is observed in the high lift vortices, widening is accelerated with increasing towing velocity. Therefore, at iso-total lift, the widening of the vortex is accelerated in the high lift configuration with respect to the reference configuration. The case of $F_z = 155N$ is an exception for the reasons stated above. For the cases where the high-lift wing is towed at $\alpha = 0^o$ (see table 4), the maximum acceleration of the widening sees a factor of 2. For the $F_z = 198N$ case where the high-lift wing is towed at $\alpha = 5.7^o$, $\Delta R_a/\Delta T$ is increased by an approximate factor of 6.

Vortices generated by an aircraft on high-lift configuration represent therefore a more significant hazard in terms of induced down-wash and rolling moment. Following eq. 5, the induced ${C_R}^{HL}$ in the axis of a vortex is affected by the increase of circulation and core radius.Consider the results for the case of iso-total lift $155N$ summarized in Table 4. For a follower aircraft of span $b_f = 0.5b_0$, 30 wingspans downstream of the leader high-lift wing the increase of circulation increases the induced rolling moment coefficient by a factor 1.5 and the widening of the core reduces it only by 3% with respect to the reference wing.

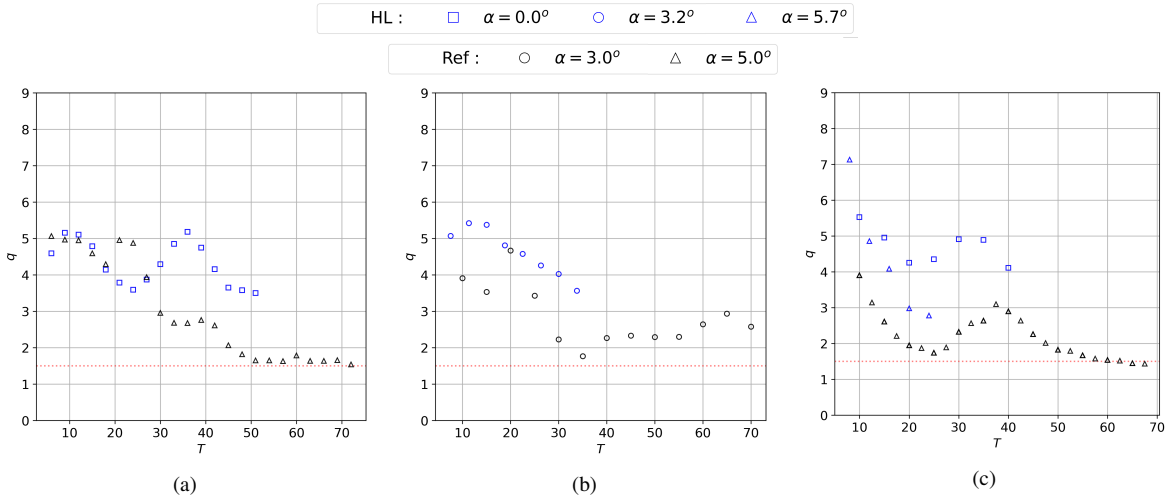

Fig. 24 Comparison of vortex swirl number at iso-total lift between the high-lift wing vortices and the reference wing vortices as a function of time, a) for $F_z = 72N$, *HL*: $U_0 = 3m/s, \alpha = 0^o$ and *Ref*: $U_0 = 3m/s, \alpha = 5^o$ b) for $F_z = 155N$, *HL*: $U_0 = 3.75m/s, \alpha = 3.2^o$ and *Ref*: $U_0 = 5m/s, \alpha = 3^o$ and d) for $F_z = 198N$, *HL*: $U_0 = 4m/s, \alpha = 5.7^o$, *HL*: $U_0 = 5m/s, \alpha = 0^o$ and *Ref*: $U_0 = 5m/s, \alpha = 5^o$,

The time evolution of the swirl number q for $F_z = 72N$, $F_z = 155N$ and $F_z = 198N$ is shown in Fig. 24. A comparison on the dynamics of the wake generated by the high-lift and reference wings is provided by the analysis of the interaction between $\overline{V_\theta}$, $\overline{V_x}$ and q. At low angles of attack, the wakes on both configurations exhibit a similar behavior. Namely, axial velocity develops slowly and non-monotonically and azimuthal velocity is quasi-constant over the time frame considered (not shown). q mirrors the non-monotonous behavior of $\overline{V_x}$, stagnating around a value higher than the unstable threshold (see Fig. 24a and Fig. 24c). As previously stated, azimuthal velocity decays and axial velocity develops with increasing angle of attack. This translates in a sharp, quasi-monotonous decrease of q until the threshold value of $q = 1.5$. The high-lift vortices exit the measurement window before q reaches 1.5, however their evolution is similar to that of the reference, suggesting that the phenomena described below would be observed on subsequent measurements. For the three cases presented in Fig. 24, once q reaches 1.5, the exchange between azimuthal and axial velocities stop, causing q to stagnate (see Fig. 24a) or oscillate (see Figs. 24b and 24c) above this threshold value. Interestingly, the increase of q (for example in *Ref*: $U_0 = 5m/s, \alpha = 5^o$ in Fig. 24c) translates into a decrease of $\overline{V_x}$ and a constant evolution of $\overline{V_\theta}$ (not shown). For all experiments considered, the vortex does not enter the unstable region of $q < 1.5$.

IV. Conclusion

An experimental study of the impact of the lift span-wise distribution (or load profile) on the vortex wake shed by a rectangular NACA 4412 wing model is described for a chord based Reynolds number of $Re_c \approx 10^5$ and circulation based Reynolds number $Re_\Gamma \approx 10^4$. These experiments are performed in a towing tank facility. Two wing model geometries are generated from a different span-wise evolution of geometrical twist to obtain two desired load profiles. The first wing, with no twist, provides a reference load profile and is representative of cruise flight. The second wing has an inboard region of constant positive twist (similar to an airplane flaps) providing a high-lift profile representative of take-off and landing flight configurations. The experiments in this work are designed to characterize the wingtip vortices as a function of towing velocity and angle of attack for each load profile. Furthermore, a comparison of the dynamics of wingtip vortices is carried out at iso-total generated lift to characterize the wake of an aircraft at the two configurations in its flight envelope. The vortex wake is investigated through stereoscopic particle image velocimetry. Specific data treatments are developed to characterize the vortex flow. Vortices exit the SPIV window at times inferior than the time scale of the Crow instability. Also, the self-induced rotation rate of the vortex was identified through the vortex location data, confirming that the Crow instability, if present, is in an early stage of development. The near-wake of the high-lift wing exhibits secondary vorticity generated by the twisted inboard section of the wing. The circulation ratio r_Γ between the two vortices shed on the same midplane of the wake is measured through the SPIV fields. Fusion time decreases with lower r_Γ. Downstream from the near-wake, the radial velocity profile $\overline{V_\theta}(r,T)$ is calculated from the vortex velocity fields by following a series of averaging steps. The diffusion of the vortex is observed through the decay of circulation and widening of the core size over time. Peak azimuthal and axial velocities evolve rapidly with respect to the decay of circulation. As peak azimuthal velocity decreases, an axial flow oriented towards the wing develops as the pressure gradient in the vortex is no longer compensated by the centrifugal forces. The swirl parameter, computed through a fit of the Batchelor model into the experimental data, decreases sharply in the early stages of vortex development, between 25 and 50 wingspans downstream of the wing. This effect is influenced by both the angle of attack and the towing velocity, as both have an incidence on the pressure drop at the vortex core. The span-wise distribution of loading does not seem to have an influence on the decrease of swirl number. The threshold value $q = 1.5$ below which helical unstable modes can develop is reached by the vortices in these experiments. However, upon reaching this value the evolution of $\overline{V_\theta}(r,T)$ and $\overline{V_x}(r,T)$ cause q to stagnate or oscillate above 1.5. The resistance of the vortex to axial destabilization has been observed by other authors in analytical and numerical works.

A high-lift span-wise distribution of ℓ_y generates the same total lift at a lower velocity or lower angle of attack with respect to the cruise flight distribution. As a product of the velocity decrease, the vortex circulation is increased in the high-lift case. The measured increase of circulation is higher than the one predicted by theoretical models. A slight increase of circulation is observed even in cases at iso-towing velocity. The decay of circulation is stronger in the high-lift configuration with respect to the reference configuration. With respect to the reference configuration, the rolling moment coefficient induced by the high-lift configuration on a follower aircraft is increased proportionally to the increase in circulation. Furthermore, the vortex core is wider in the wake of the high-lift configuration and its widening is accelerated with respect to the reference configuration. The widening of the core is accelerated in configurations that promote the development of axial flow. With respect to the reference configuration, the induced rolling moment coefficient is reduced by the wider core sizes in the high lift wake. However, the sensitivity of C_R to the widening of the vortex is a function of the ratio between the span of the follower aircraft and the vortex core size. For most practical applications, in terms of induced C_R the wider vortex core in the high-lift configuration does not compensate for its higher vortex circulation.

In future work, the measurement window will be adapted to study the wake at larger downstream stations ($T_C > 0.7$). These experiments will aim to characterize the development of the Crow instability. Additionally, the characterization of the vortex behavior when the swirl number stagnates around the value of 1.5 is of interest and requires measurements further downstream. The orientation and length of the inboard twisted region of the wing model will then be modified to observe the dynamics of 4-vortex systems and characterize the onset of cooperative instabilities.

V. Acknowledgments

The authors would like to thank Yves Le-Sant for its help regarding SPIV post-processing software and Pierre Saulgeot for his commentaries on the analysis of vortex fusion.

References

[1] Betz, A., "Verhalten von Wirbelsystemen," *ZAMM - Journal of Applied Mathematics and Mechanics / Zeitschrift für Angewandte Mathematik und Mechanik*, Vol. 12, No. 3, 1932, pp. 164–174. https://doi.org/10.1002/zamm.19320120307.

[2] Condit, P. M., and Tracy, P. W., "Results of the Boeing Company Wake Turbulence Test Program," *Aircraft Wake Turbulence and Its Detection*, Springer US, Boston, MA, 1971, pp. 473–508. https://doi.org/10.1007/978-1-4684-8346-8_25.

[3] Crow, S., "Stability Theory for a Pair of Trailing Vortices," *AIAA Journal*, Vol. 8, No. 12, 1970, pp. 2172–2179. https://doi.org/https://doi.org/10.2514/3.6083.

[4] Tsai, C. Y., and Widnall, S. E., "The stability of short waves on a straight vortex filament in a weak externally imposed strain field," *Journal of Fluid Mechanics*, Vol. 73, No. 4, 1976, pp. 721–733. https://doi.org/10.1017/S0022112076001584.

[5] Roy, C., Leweke, T., Thompson, M. C., and Hourigan, K., "Experiments on the elliptic instability in vortex pairs with axial core flow," *Journal of Fluid Mechanics*, Vol. 677, 2011, pp. 383–416. https://doi.org/10.1017/jfm.2011.91.

[6] Leweke, T., and Williamson, C. H., "Experiments on long-wavelength instability and reconnection of a vortex pair," *Physics of Fluids*, Vol. 23, No. 2, 2011. https://doi.org/10.1063/1.3531720.

[7] Meunier, P., Le Dizès, S., and Leweke, T., "Physics of vortex merging," *Comptes Rendus Physique*, Vol. 6, No. 4-5 SPEC. ISS., 2005, pp. 431–450. https://doi.org/10.1016/j.crhy.2005.06.003.

[8] Devenport, W. J., Zsoldos, J. S., and Vogel, C. M., "The structure and development of a counter-rotating wing-tip vortex pair," *Journal of Fluid Mechanics*, Vol. 332, 1997, pp. 71–104. https://doi.org/10.1017/s0022112096003795.

[9] Brion, V., and Jacquin, L., "Measurements of a turbulent vortex pair using time resolved PIV," *6th AIAA Theoretical Fluid Mechanics Conference*, 2011, pp. 1–15. https://doi.org/10.2514/6.2011-3892.

[10] Ortega, J. M., "Stability characteristics of counter-rotating vortex pairs in the wakes of triangular-flapped airfoils," Ph.D. thesis, University of California, Berkeley, 2001.

[11] Crouch, J. D., "Instability and transient growth for two trailing-vortex pairs," *35th Aerospace Sciences Meeting and Exhibit*, Vol. 350, 1997, pp. 311–330. https://doi.org/10.2514/6.1997-62.

[12] Fabre, D., and Jacquin, L., "Stability of a four-vortex aircraft wake model," *Physics of Fluids*, Vol. 12, No. 10, 2000, pp. 2438–2443. https://doi.org/10.1063/1.1289397.

[13] Fabre, D., Jacquin, L., and Loof, A., "Optimal perturbations in a four-vortex aircraft wake in counter-rotating configuration," *Journal of Fluid Mechanics*, Vol. 451, 2002, pp. 319–328. https://doi.org/10.1017/s0022112001006954.

[14] Bristol, R. L., Ortega, J. M., Marcus, P. S., and Savaş, Ö., "On cooperative instabilities of parallel vortex pairs," *Journal of Fluid Mechanics*, 2004. https://doi.org/10.1017/S0022112004001016.

[15] Durston, D. A., Walker, S. M., Driver, D. M., Smith, S. C., and Savaş, Ö., "Wake-vortex alleviation flowfield studies," *Journal of Aircraft*, Vol. 42, No. 4, 2005, pp. 894–907. https://doi.org/10.2514/1.7904.

[16] Breitsamter, C., "Wake vortex characteristics of transport aircraft," *Progress in Aerospace Sciences*, Vol. 47, No. 2, 2011, pp. 89–134. https://doi.org/10.1016/j.paerosci.2010.09.002.

[17] Batchelor, G., "Axial flow in trailing line vortices," *Journal of Fluid Mechanics*, Vol. 20, No. 4, 1964, pp. 645–658.

[18] Moore, D., and Saffman, P. G., "Axial flow in laminar trailing vortices," *Proceedings of the Royal Society of London. A. Mathematical and Physical Sciences*, Vol. 333, No. 1595, 1973, pp. 491–508. https://doi.org/10.1098/rspa.1973.0075.

[19] Moet, H., Laforte, F., and Poinsot, T., "Wave propagation in vortices and vortex bursting," *Physics of Fluids*, Vol. 17, No. 5, 2005, pp. 1–15. https://doi.org/10.1063/1.1896937.

[20] Meunier, P., "Etude expérimentale de deux tourbillons corotatifs," Ph.D. thesis, Université de Provence Aix-Marseille I, 2001.

[21] Lessen, M., and Paillet, F., "The stability of a trailing line vortex. Part 2. Viscous theory," *Journal of Fluid Mechanics*, Vol. 65, No. 4, 1974, pp. 769–779. https://doi.org/10.1017/S0022112074001649.

[22] Mayer, E. W., and Powell, K. G., "Viscous and inviscid instabilities of a trailing vortex," *Journal of Fluid Mechanics*, Vol. 245, 1992, pp. 91–114. https://doi.org/10.1017/S0022112092000363.

[23] Delbende, I., Chomaz, J.-M., and Huerre, P., "Absolute/convective instabilities in the Batchelor vortex: a numerical study of the linear impulse response," *Journal of Fluid Mechanics*, Vol. 355, 1998, pp. 229–254.

[24] Olendraru, C., Sellier, A., Rossi, M., and Huerre, P., "Inviscid instability of the Batchelor vortex: Absolute-convective transition and spatial branches," *Physics of Fluids*, Vol. 11, No. 7, 1999, pp. 1805–1820. https://doi.org/10.1063/1.870045.

[25] Glauert, H., *The Elements of Aerofoil and Airscrew Theory*, Cambridge University Press, 1926.

[26] Rossow, V. J., "On the Inviscid Rolled-Up Structure of Lift-Generated Vortices," *Journal of Aircraft*, Vol. 1, No. November, 1973, pp. 647–650.

[27] Spalart, P. R., "Airplane trailing vortices," *Annual Review of Fluid Mechanics*, Vol. 30, 1998, pp. 107–138. https://doi.org/10.1146/annurev.fluid.30.1.107.

[28] Gerz, T., Holzäpfel, F., and Darracq, D., "Commercial aircraft wake vortices," *Progress in Aerospace Sciences*, Vol. 38, No. 3, 2002, pp. 181–208. https://doi.org/10.1016/S0376-0421(02)00004-0.

[29] Savaş, Ö., "Experimental investigations on wake vortices and their alleviation," , 2005. https://doi.org/10.1016/j.crhy.2005.05.004.

[30] Brion, V., Sipp, D., and Jacquin, L., "Optimal amplification of the Crow instability," *Physics of Fluids*, Vol. 19, No. 11, 2007. https://doi.org/10.1063/1.2793146.

[31] Edstrand, A. M., Sun, Y., Schmid, P. J., Taira, K., and Cattafesta, L. N., "Active attenuation of a trailing vortex inspired by a parabolized stability analysis," *Journal of Fluid Mechanics*, Vol. 855, 2018, pp. 1–12. https://doi.org/10.1017/jfm.2018.701.

[32] Navrose, Brion, V., and Jacquin, L., "Transient growth in the near wake region of the flow past a finite span wing," *Journal of Fluid Mechanics*, Vol. 866, 2019, pp. 399–430. https://doi.org/10.1017/jfm.2019.110.

[33] Cruz Marquez, R., Monnier, J. C., Tanguy, G., Couliou, M., Brion, V., Cattafesta, L., and Dupont, P., "An experimental study of a trailing vortex alleviation using an undulated trailing edge," *AIAA Aviation Forum*, 2021, pp. 1–18. https://doi.org/10.2514/6.2021-2562.

[34] Dghim, M., Ferchichi, M., and Fellouah, H., "Mid-wake wing tip vortex dynamics with active flow control," *Experimental Thermal and Fluid Science*, Vol. 98, 2018, pp. 38–55. https://doi.org/10.1016/j.expthermflusci.2018.05.011.

[35] Guha, T. K., and Kumar, R., "Characteristics of a wingtip vortex from an oscillating winglet," *Experiments in Fluids*, Vol. 58, No. 1, 2017. https://doi.org/10.1007/s00348-016-2289-3.

[36] Brossard, C., Monnier, J.-C., Barricau, P., Vandernoot, F.-X., Sant, Y. L., Champagnat, F., and Besnerais, G. L., "Principles and applications of particle image velocimetry," *Onera AerospaceLab Journal*, Vol. 1, 2009, pp. 1–11.

[37] Champagnat, F., Plyer, A., Le Besnerais, G., Leclaire, B., Davoust, S., and Le Sant, Y., "Fast and accurate PIV computation using highly parallel iterative correlation maximization," *Experiments in Fluids*, Vol. 50, No. 4, 2011, pp. 1169–1182. https://doi.org/10.1007/s00348-011-1054-x.

[38] Besnerais, G. L., and Champagnat, F., "Dense optical flow by iterative local window registration," *Proceedings - International Conference on Image Processing, ICIP*, 2005. https://doi.org/10.1109/ICIP.2005.1529706.

[39] Spreiter, J. R., and Sacks, A. H., "The Rolling Up of the Trailing Vortex Sheet and Its Effect on the Downwash Behind Wings," *Journal of the Aeronautical Sciences*, Vol. 18, No. 1, 1951, pp. 21–32. https://doi.org/10.2514/8.1830.

[40] Fabre, D., *Instabilités et instationnarités dans les tourbillons applications aux sillages d'avions*, 1st ed., ONERA, Chatillon, 2002.

[41] Graftieaux, L., Michard, M., and Grosjean, N., "Combining PIV, POD and vortex identification algorithms for the study of unsteady turbulent swirling flows," *Measurement Science and Technology*, Vol. 12, No. 9, 2001, pp. 1422–1429. https://doi.org/10.1088/0957-0233/12/9/307.

[42] Saffman, P. G., *Vortex Dynamics*, Cambridge University Press, 1992. https://doi.org/10.1017/CBO9780511624063.

[43] Doligalski, T. L., Smith, C. R., and Walker, J. D. A., "Vortex Interactions With Walls," *Annual Review of Fluid Mechanics*, Vol. 26, 1994, pp. 573–616. https://doi.org/https://doi.org/10.1146/annurev.fl.26.010194.003041.

[44] Murphy, J., "Intake Ground Vortex Aerodynamics," Ph.D. thesis, Cranfield University, 2008. URL http://hdl.handle.net/1826/3515.

[45] McLelland, G., "Aerodynamics of vortex ingestion for aero-engines," Ph.D. thesis, Cranfield University, 2013.

[46] Hallock, J. N., and Burnham, D. C., "Decay characteristics of wake vortices from jet transport aircraft," *35th Aerospace Sciences Meeting and Exhibit*, 1997. https://doi.org/10.2514/6.1997-60.

[47] Jacquin, L., and Pantano, C., "On the persistence of trailing vortices," *Journal of Fluid Mechanics*, Vol. 471, 2002, pp. 159–168. https://doi.org/10.1017/S0022112002002161.

[48] Ragab, S., and Sreedhar, M., "Numerical simulation of vortices with axial velocity deficits," *Physics of Fluids*, Vol. 7, No. 549, 1995. https://doi.org/https://doi.org/10.1063/1.868582.

[49] Rossow, V. J., "Extended-Betz methods for roll-up of vortex sheets," *Journal of Aircraft*, Vol. 34, No. 5, 1997, pp. 592–599. https://doi.org/10.2514/2.2234.